Simulating a Gaussian stochastic gravitational wave background signal in pulsar timing arrays

Reginald Christian Bernardo[1,2,*] and Kin-Wang Ng[3,4,†]

[1]Max Planck Institute for Gravitational Physics (Albert Einstein Institute), Hannover D-30167, Germany
[2]Asia Pacific Center for Theoretical Physics, Pohang 37673, Korea
[3]Institute of Physics, Academia Sinica, Taipei 11529, Taiwan
[4]Institute of Astronomy and Astrophysics, Academia Sinica, Taipei 11529, Taiwan

(Received 7 August 2025; accepted 21 January 2026; published 11 February 2026)

We revisit the theoretical modeling and simulation of a Gaussian stochastic gravitational wave background (SGWB) signal in a pulsar timing array (PTA). We show that the correlation between Fourier components of pulsar timing residuals can be expressed using transfer functions; that are indicative of characteristic temporal correlations in a SGWB signal observed in a finite time window. These transfer functions, when convolved with the SGWB power spectrum and spatial correlation (Hellings and Downs curve), describe the variances and correlations of the pulsar timing residuals' Fourier coefficients. The convolutions are the exact frequency- and Fourier-domain representations of the time-domain covariance function. We derive explicit forms for the transfer functions for unpolarized and circularly polarized SGWB signals. We validate our results by comparing Gaussian theoretical expectation values with standard simulations based on point sources and our own covariance-matrix-based approach. The unified frequency- and Fourier-domain formalism provides a robust foundation for future PTA precision analyses and highlights the importance of temporal correlations in interpreting GW signals.

DOI: 10.1103/gv4z-sdp2

I. INTRODUCTION

The compelling evidence of a nanohertz stochastic gravitational wave background (SGWB) provided by pulsar timing arrays (PTAs) [1–5] is a milestone in gravitational wave (GW) astronomy [6–8]. Unlike the signals captured by ground-based GW detectors, which originate from individual compact binary mergers, the leading GW signal observed by PTAs is expected to arise from the incoherent superposition of GWs emitted by a vast population of sources, each too weak to be individually resolved [9–19]. While searches for a SGWB in the hectohertz regime remain a primary goal of ground-based detectors, and similar efforts are planned in the millihertz band by future space-based observatories [20–27], the primary source of the SGWB may vary across frequency bands. In the nanohertz regime accessible to PTAs, the dominant contribution is widely considered to come from an astrophysical population of supermassive black hole binaries (SMBHBs) [28–43], producing the characteristic Hellings and Downs (HD) correlation [44–46]. However, uncertainties in the observed signal's spectrum leave room for a variety of alternative interpretations, including scenarios involving beyond-standard-model cosmological processes [47–93].

The ability of PTAs to constrain the SGWB through timing data improves with the inclusion of additional millisecond pulsars and longer observation times [25,34,94,95]. A natural path forward is to continue expanding current PTA experiments, increasing sky coverage and sensitivity to refine our understanding of the signal's origin. At the same time, it is crucial to revisit the theoretical foundations of the analysis [96–111], utilizing simulations and improved data processing techniques to extract physical insights while mitigating statistical and systematic uncertainties [112–118]. This paper follows the latter approach by revisiting the theoretical framework of a Gaussian SGWB signal in the frequency- and Fourier-domain,[1] providing a perspective that complements

*Contact author: reginald.christian.bernardo@aei.mpg.de
†Contact author: nkw@phys.sinica.edu.tw

Published by the American Physical Society under the terms of the Creative Commons Attribution 4.0 International license. Further distribution of this work must maintain attribution to the author(s) and the published article's title, journal citation, and DOI. Open access publication funded by the Max Planck Society.

[1]We are reminding the subtle distinction between the terms frequency- and Fourier-domains, since a random signal can always be interpreted in the frequency-domain with an arbitrary choice of orthogonal basis vectors other than with sines and cosines. See [119] for an example of using a Legendre polynomial basis to look into PTA signals.

the time-domain methods commonly adopted in PTA analyses.

A Gaussian reference model provides a meaningful baseline for analyzing stochastic signals. In cosmology, the cosmic microwave background (CMB) serves as a prime example: standard inflation predicts nearly Gaussian primordial fluctuations, and deviations from this baseline may point to new physics such as nonstandard inflation or late-time effects like lensing [120,121]. The Gaussian model thus defines a null hypothesis, against which any statistically significant deviations can be tested for physical implications. A similar logic applies to PTAs, where a Gaussian SGWB is typically assumed as a starting point in both theoretical modeling and data analysis. However, unlike the CMB, where the signal dominates over noise, PTAs face the challenge of identifying weak signals amid strong pulsar-intrinsic red noise [122] and other systematics. Despite this, establishing and testing the Gaussian null hypothesis remains a promising approach—it may uncover subtle statistical imprints that help distinguish between astrophysical and cosmological origins of the SGWB. This motivates a careful reexamination of the signal's statistical structure, particularly how Gaussianity manifests in correlations and spectral features.

A (Universe-age old) question we address in this work is: given that a SGWB source emits over a broad range of frequencies with a characteristic timescale of order of a million to a billion years, how can such a signal be characterized observationally when the PTA baseline is only a few decades? The answer has been provided in Ref. [108], and later in Refs. [117,118]. A signal with such a characteristic time scale would have made a very large number of cycles and have continuous support at all frequencies in the observation band. Any Fourier basis with a discrete set of frequencies determined by the observation time scale is inevitably misaligned with the signal's intrinsic harmonics, leading to correlations among frequency components.

Building on Ref. [117], we show that the correlation of the Fourier coefficients of pulsar timing residuals can be expressed using "transfer functions".[2] In general, transfer functions describe how intrinsic properties of a signal map onto observable quantities. In PTAs, they encode temporal correlations due to GW propagation in time and frequency correlations induced by observing the signal in a finite time window.[3] As we demonstrate, this structure manifests in the frequency- and Fourier-domain as a convolution between the power spectrum and the transfer functions [108,117]. In this work, we derive the transfer functions for both isotropic unpolarized [Eqs. (22)-(23)] and circularly polarized [Eq. (67)] SGWB signals in a PTA. We validate the theoretical expectation values for a Gaussian SGWB by their agreement with standard numerical simulations of a GW signal produced by a finite number of point sources [126] and with our own covariance-matrix-based simulations. These results clarify how Gaussian SGWB signals whether unpolarized or circularly polarized should be modeled within the PTA observation window. This, in turn, enables more efficient simulations and lays a foundational step toward testing the Gaussianity of the SGWB signal and possibly utilizing simulation-based inference methods in PTA science.

The remainder of this paper is organized as follows. Section II provides a brief summary of the standard interpretation of the SGWB signal in terms of the Fourier coefficients of pulsar timing residuals. In Sec. III, we present our first main result: by revisiting the derivation of the pulsar timing residual correlation [Eq. (14)], we extract the correlations between Fourier coefficients, leading to transfer functions. Section IV introduces a numerical framework for simulating a Gaussian SGWB and validates our analytical predictions against ensemble-averaged quantities from both theoretical expectations and standard point-source based PTA simulations. In Sec. V, we extend our analysis to accommodate a circularly polarized SGWB, and further validate these results through simulation in Sec. VI, highlighting subtleties related to the computational frame [127–131]. Then, in Sec. VII, we provide a brief discussion of what we think are the most conceptually interesting aspects of the work. Finally, Sec. VIII summarizes our main findings and outlines directions for future work.

Appendix A establishes the equivalence between the sine-cosine and exponential interpretations of a time series through the Fourier components of the timing residual correlation and the corresponding transfer functions. Appendix B collects useful spherical harmonic identities. Appendix C details our procedure for simulating a Gaussian SGWB signal in PTAs based on covariance matrices and Gaussian random variables. Appendix D presents results for varying the number of pulsars in a PTA. Appendix E provides a quick recipe for computing the elements of the covariance matrix in the frequency- and Fourier-domain.

Throughout this work, we adopt the mostly plus metric signature $(-,+,+,+)$ and use geometrized units with $G = c = 1$. Pulsars are indexed by lowercase Latin letters a, b, and frequency bins by j, k. For brevity, we denote $\langle X_{aj} Y_{bk} \rangle \equiv \langle X_j(\hat{e}_a) Y_k(\hat{e}_b) \rangle$ where $X_j(\hat{e}_a)$ and $Y_k(\hat{e}_b)$ are the Fourier coefficients of the timing residuals in directions $\hat{e}_a$ and $\hat{e}_b$, respectively [cf. Eq. (1)], and $\langle \cdots \rangle$ denotes ensemble averaging.

[2]Filters are suggestive of a function chosen to suit ones purposes, e.g., polaroid. Instead the ones introduced in Ref. [117] are a property of any time correlated process. Hence, we are now calling them transfer functions. We thank Bruce Allen for the suggestion.

[3]Misconceptions in the community [123–125] lead to a dismissal of the significance of the temporal correlation [96,97].

II. TIMING RESIDUAL ANALYSIS IN THE FREQUENCY- AND FOURIER-DOMAIN

The pulsar timing residual can be written as a Fourier series[4] [16,132],

$$r(t,\hat{e}) = \frac{\alpha_0(\hat{e})}{2} + \sum_{k=1}^{\infty} \alpha_k(\hat{e}) \sin(\omega_k t) + \sum_{k=1}^{\infty} \beta_k(\hat{e}) \cos(\omega_k t), \tag{1}$$

where $\omega_k = 2\pi f_k$, $f_k = k/T$, k is a positive integer, T is the total observation time, and $\hat{e}$ is the unit vector pointing in the pulsar's direction. Then, the Fourier components of the timing residual are given by[5]

$$\begin{aligned} \alpha_0(\hat{e}) &= \frac{2}{T}\int_0^T dt\, r(t,\hat{e}), \\ \alpha_j(\hat{e}) &= \frac{2}{T}\int_0^T dt\, r(t,\hat{e}) \sin(\omega_j t), \\ \beta_j(\hat{e}) &= \frac{2}{T}\int_0^T dt\, r(t,\hat{e}) \cos(\omega_j t). \end{aligned} \tag{2}$$

PTAs measure the spectrum of the signal at discrete frequencies $f_k = k/T = kf_1$, where T is the total observation time. For $T \sim n_{\rm yr}$ years, the lowest accessible frequency is $f_1 \sim 31.8/n_{\rm yr}$ nHz. In contrast, the characteristic time scale of the stochastic GW signal is much longer, $T_{\rm gw} \sim 10^9$ years. The transfer functions (22)–(23) and (67) determine how a broadband signal is mapped onto the α- and β-observational Fourier bins of the timing residual correlation. Crucially, these transfer functions are *not* Kronecker deltas; instead, their finite width means that each observed frequency bin receives contributions from a broad range of frequencies. This leads to interfrequency correlations, which must be accounted for in PTA analyses. For a discussion of the observational implications, see Refs. [108,117,118] and Sec. VII.

III. THE UNPOLARIZED SIGNAL: SPECTRUM × HD CURVE × TRANSFER FUNCTIONS

In this section, we rederive the SGWB signal and correlation in the pulsar timing residuals.

A. Pulsar timing residual from GWs

We begin by considering a stochastic superposition of GWs, characterized by various frequencies f and propagation directions $\hat{k}$

$$h_{ij}(\eta,\vec{x}) = \sum_{A=+,\times} \int_{-\infty}^{\infty} df \int_{S^2} d\hat{k} \times h_A(f,\hat{k}) \varepsilon_{ij}^A e^{-2\pi i f(\eta - \hat{k}\cdot\vec{x})}, \tag{3}$$

where η denotes conformal time, $\vec{x}$ represents the position vector, and ε_{ij}^+ and $\varepsilon_{ij}^\times$ are the transverse-traceless polarization basis tensors. Here h_{ij} is real; its Fourier components satisfy $h_A(-f,\hat{k}) = h_A^*(f,\hat{k})$. We define a SGWB as a collection of GWs such that h_{ij} are Gaussian random fields with a statistical behavior completely characterized by the two-point correlation function, $\langle h_{ij}(\eta,\vec{x}_1) h_{kl}(\eta,\vec{x}_2)\rangle$, where angle brackets denote ensemble averages.

For a GW propagating along a direction $\hat{k}$, the polarization tensors can be written as $\varepsilon^+ = \hat{m}\otimes\hat{m} - \hat{n}\otimes\hat{n}$ and $\varepsilon^\times = \hat{m}\otimes\hat{n} + \hat{n}\otimes\hat{m}$, where $(\hat{m},\hat{n},\hat{k})$ form an orthonormal triad [135]. The influence of a GW on pulsar timing residuals, $r(t,\hat{e})$, can be expressed as an integral over redshift space fluctuations, $z(t,\hat{e})$

$$r(t,\hat{e}) = \int_0^t dt' z(t',\hat{e}), \tag{4}$$

where t is the time of observation. Note that this considers the GW effects in the locations of the Earth and the pulsar; traditionally referred to as Earth and pulsar terms, respectively. It is worth pointing out that the HD curve is derived from the Earth term. For a GW, such as $h_{ij}(\eta,\vec{x})$ given by Eq. (3), with photons emitted at conformal time η_e and received at η_r, the redshift space fluctuation can be described by a Sachs-Wolfe integral [136]

$$z(t',\hat{e}) = -\frac{1}{2}\int_{t'+\eta_e}^{t'+\eta_r} d\eta \hat{e}^i \hat{e}^j \partial_\eta h_{ij}(\eta,\vec{x}). \tag{5}$$

Here, $\hat{e}^i \otimes \hat{e}^j$ is commonly referred to as a detector tensor.

By substituting Eq. (3) into Eqs. (4)–(5), we obtain

$$r(t,\hat{e}) = \int_0^t dt' \int_{t'+\eta_e}^{t'+\eta_r} d\eta \sum_A \int_{-\infty}^{\infty} df \times \int_{S^2} d\hat{k} \pi i f \hat{e}^i \hat{e}^j h_A(f,\hat{k}) \varepsilon_{ij}^A(\hat{k}) e^{-2\pi i f(\eta - \hat{k}\cdot\vec{x})}. \tag{6}$$

Then, by expanding the plane wave in spherical harmonics and performing the integrals over t' and η, we find the expression of the pulsar timing residual as a harmonic series,

[4] An equivalent way to write the Fourier series of the timing residual is $r(t,\hat{e}) = \sum_{k=-\infty}^{\infty} c_k(\hat{e}) e^{i\omega_k t}$ [108]. See Appendix A.

[5] In PTA analysis [133,134], the Fourier coefficients are inferred by Bayesian parameter estimation, accounting for marginalization over the Fourier mode phases and spectral leakage mitigation through fitting to pulsar spin frequency and its first derivative, which are expected to make variances equal. The Bayesian inferred coefficients are generally different compared to Eq. (2) which are the mathematically exact inverse transform of the linear operation (1) when interpreting a stochastic process in a finite time window.

$$r(t,\hat{e}) = \sum_{lm} a_{lm}(t) Y_{lm}(\hat{e}), \tag{7}$$

where the coefficients $a_{lm}(t)$'s are given by

$$a_{lm}(t) = \sum_{A=+,\times} \int_{-\infty}^{\infty} d\omega \int_{S^2} d\hat{k}(1-e^{-i\omega t}) \left(\frac{e^{-i\omega\eta_r}}{\omega}\right) \times \hat{e}^i \hat{e}^j h_A\left(\frac{\omega}{2\pi},\hat{k}\right) \varepsilon^A_{ij}(\hat{k}) \int_0^{\omega D} dx e^{ix} i^l j_l(x) Y^*_{lm}(\hat{k}), \tag{8}$$

$\omega = 2\pi f$ is the angular frequency, and $j_l(x)$'s are the spherical Bessel functions of the first kind.

We use this result to compute the pulsar timing residual correlation.

B. Timing residual correlation due to a SGWB

We consider a standard Gaussian, isotropic, and stationary SGWB; in symbols, we write down

$$\langle h_A(f,\hat{k}) h^*_{A'}(f',\hat{k}')\rangle = I(f)\delta_{AA'}\delta(f-f')\delta(\hat{k},\hat{k}'), \tag{9}$$

where $I(f)$ is the SGWB power spectrum. The Dirac delta functions are dictated by temporal and spatial translational invariance.

Using Eqs. (7)–(8), we can express the timing residual cross correlation between a pair of pulsars to be

$$\langle r(t_a,\hat{e}_a) r(t_b,\hat{e}_b)\rangle = \sum_{l_1m_1}\sum_{l_2m_2} \langle a_{l_1m_1}(t_a) a^*_{l_2m_2}(t_b)\rangle Y_{l_1m_1}(\hat{e}_a) Y^*_{l_2m_2}(\hat{e}_b), \tag{10}$$

where

$$\langle a_{l_1m_1}(t_a) a^*_{l_2m_2}(t_b)\rangle = \int_{-\infty}^{\infty} \frac{df}{(2\pi f)^2} C(f,t_a,t_b) \times \sum_{A_1A_2} \int_{S^2} d\hat{k} I(f) J^{A_1}_{l_1m_1}(fD_a,\hat{k}) J^{A_2*}_{l_2m_2}(fD_b,\hat{k}), \tag{11}$$

$$C(f,t_a,t_b) = (1-e^{-2\pi i f t_a})(1-e^{2\pi i f t_b}), \tag{12}$$

and

$$J^A_{lm}(fD,\hat{k}) = 2\pi \int_0^{2\pi fD} dx e^{ix} \sum_{LM} i^L Y^*_{LM}(\hat{k}) j_L(x) \times \int_{S^2} d\hat{e}\hat{e}^i\hat{e}^j \varepsilon^A_{ij}(\hat{k}) Y_{LM}(\hat{e}) Y^*_{lm}(\hat{e}). \tag{13}$$

Then, after straightforward manipulation, we obtain the timing residual correlation as

$$\langle r(t_a,\hat{e}_a) r(t_b,\hat{e}_b)\rangle = \int_0^{\infty} \frac{2df}{(2\pi f)^2} \mathrm{Re}[C(f,t_a,t_b)] I(f) \times \sum_{A=+,\times} \gamma^A(fD_a,fD_b,\hat{e}_a\cdot\hat{e}_b), \tag{14}$$

where the $\gamma^A(fD_a,fD_b,\hat{e}_a\cdot\hat{e}_b)$'s are given by

$$\gamma^A(fD_a,fD_b,\hat{e}_a\cdot\hat{e}_b) = \sum_{l_1m_1}\sum_{l_2m_2} Y_{l_1m_1}(\hat{e}_a) Y^*_{l_2m_2}(\hat{e}_b) \times \int_{S^2} d\hat{k} Y_{00}(\hat{k}) J^A_{l_1m_1}(fD_a,\hat{k}) J^{A*}_{l_2m_2}(fD_b,\hat{k}). \tag{15}$$

The timing residual cross correlation between a pair of pulsars depends only on the angular separation. The angular dependence, $\hat{e}_a\cdot\hat{e}_b$, depending only upon on the relative positions of pulsars with one another, is reflective of isotropy; $\gamma(fD_a,fD_b,\hat{e}_a,\hat{e}_b) \equiv \gamma(fD_a,fD_b,\hat{e}_a\cdot\hat{e}_b)$. The above result (14) shows that the SGWB signal in the timing residual correlation has three parts: a time-frequency kernel $C(f,t,t')$, a power spectrum, $I(f)$, and a spatial correlation (HD curve), $\gamma(fD_a,fD_b,\hat{e}_a\cdot\hat{e}_b)$. Setting apart the terms associated with the lower limit of the integral (4) (which fixes the initial phase of the timing residuals), the result (14) could be read as a statement of the Wiener-Khinchin theorem for a stationary stochastic process. We emphasize that the temporal correlation $C(f,t,t')$ is associated with the GW propagation in time. Implications of this factor for interpreting a SGWB observation in PTAs were discussed in Ref. [117].

Adding to our last thought, we may remind that a stationary colored process with a covariance function $C(|t-t'|)$ at two different times $t \neq t'$ can be described by the Wiener-Khinchin theorem: $C(\tau) = \int df S(f)\cos(2\pi f\tau)$. This can be derived by treating the signal in the Fourier basis. In a physical process, such as GWs that behave as $h \sim \exp(-i(\omega t - \vec{k}\cdot\vec{x}))$ apart from the $+$ and $\times$ polarization tensors, the Wiener-Khinchin theorem is realized through a large sum of deterministic contributions that render the description of the overall signal a statistical sense. Part of what gives the stochastic signal its temporally correlated behavior are the phase factors $\exp(-i\omega t)$ which describe a physical wave's temporal propagation; e.g., the oscillating motion of an infinitesimal piece of a vibrating drum.

For general relativity and most of this work, the spatial correlation can be regarded as simply the HD curve,

$$\sum_{A=+,\times} \gamma^A(fD_a,fD_b,\hat{e}_a\cdot\hat{e}_b) \sim \gamma^{\mathrm{HD}}(\hat{e}_a\cdot\hat{e}_b) = \bar{\mathcal{N}} \times \left(\mathbf{\Gamma}(\hat{e}_a\cdot\hat{e}_b) + \frac{\delta_{ab}}{2}\right), \tag{16}$$

where $\bar{\mathcal{N}}$ is a constant and $\mathbf{\Gamma}(x)$ is

$$\mathbf{\Gamma}(x) = \frac{1}{2} - \frac{1}{4}\left(\frac{1-x}{2}\right) + \frac{3}{2}\left(\frac{1-x}{2}\right)\ln\left(\frac{1-x}{2}\right). \quad (17)$$

This approximation holds well in the long arm limit [46,137], valid for PTAs where the wavelength of GWs are $\lambda_{\rm gw} \sim \mathcal{O}(1)$ pc and the distances to the pulsars are $D \sim \mathcal{O}(1)$ kpc. The term δ_{ab} in Eq. (16) is added *ad hoc* to account for the power at small angular scales. A derivation of the spatial correlation starting with Eq. (15) can found in Refs. [100,132], among other recent references [45,98,138,139]. The quantities $\gamma(x_a, x_b, \cos\theta)$ and $\mathbf{\Gamma}(\cos\theta)$ pertaining to spatial correlation in PTA are referred to as ORFs.

C. Transfer functions

When reading the timing residual data as Eq. (1), the SGWB signal (14) can be interpreted as a convolution between the power spectrum, $I(f)$, the spatial correlation, $\gamma(fD_a, fD_b, \hat{e}_a \cdot \hat{e}_b)$, and transfer functions, tailored to each frequency bin and Fourier component of the correlation [108,117].

We derive the transfer functions in the following. Using Eq. (14), for the $\langle\alpha_{aj}\alpha_{bk}\rangle$ and $\langle\beta_{aj}\beta_{bk}\rangle$ components, we obtain

$$\begin{aligned}\langle\alpha_{aj}\alpha_{bk}\rangle &\equiv \left(\frac{2}{T}\right)^2 \iint_0^T dt dt' \langle r(t,\hat{e}_a) r(t',\hat{e}_b)\rangle \sin(\omega_j t)\sin(\omega_k t') \\ &= \int_{f_{\rm min}}^{f_{\rm max}} \frac{2df}{(2\pi f)^2} \mathcal{C}^{\alpha}_{j,k}(f) I(f) \gamma(fD_a, fD_b, \hat{e}_a, \hat{e}_b), \end{aligned} \quad (18)$$

$$\begin{aligned}\langle\beta_{aj}\beta_{bk}\rangle &\equiv \left(\frac{2}{T}\right)^2 \iint_0^T dt dt' \langle r(t,\hat{e}_a) r(t',\hat{e}_b)\rangle \cos(\omega_j t)\cos(\omega_k t') \\ &= \int_{f_{\rm min}}^{f_{\rm max}} \frac{2df}{(2\pi f)^2} \mathcal{C}^{\beta}_{j,k}(f) I(f) \gamma(fD_a, fD_b, \hat{e}_a, \hat{e}_b), \end{aligned} \quad (19)$$

where we use the notation $\iint_0^T = \int_0^T \int_0^T$ for the double integral, and the transfer functions, $\mathcal{C}^{\alpha}_{j,k}(f)$ and $\mathcal{C}^{\beta}_{j,k}(f)$, have been defined as

$$\mathcal{C}^{\alpha}_{j,k}(f) = \left(\frac{2}{T}\right)^2 \iint_0^T dt\, dt' {\rm Re}[C(f,t,t')] \sin(\omega_j t)\sin(\omega_k t'), \quad (20)$$

$$\mathcal{C}^{\beta}_{j,k}(f) = \left(\frac{2}{T}\right)^2 \iint_0^T dt\, dt' {\rm Re}[C(f,t,t')] \cos(\omega_j t)\cos(\omega_k t'). \quad (21)$$

The integral limits have been truncated at $f_{\rm min} \sim 1/T$ to $f_{\rm max} = \mathcal{O}(10)/T$ to correspond to the PTA sensitivity range. By substituting (12), we obtain[6]

$$\mathcal{C}^{\alpha}_{j,k}(f) = \frac{4 f_j f_k}{\pi^2 T^2} \frac{\sin^2(\pi f T)}{(f^2 - f_j^2)(f^2 - f_k^2)}, \quad (22)$$

$$\mathcal{C}^{\beta}_{j,k}(f) = \frac{4 f^2}{\pi^2 T^2} \frac{\sin^2(\pi f T)}{(f^2 - f_j^2)(f^2 - f_k^2)}. \quad (23)$$

As the name suggests, the transfer functions, $\mathcal{C}^{\alpha}_{jk}(f)$ and $\mathcal{C}^{\beta}_{jk}(f)$, carry the properties of the signal to the observable quantity, or in this case the Fourier components of the timing residual correlation [117].

It is worth mentioning that the important piece of the temporal correlation (12) that gives Eqs. (22)–(23) is the last term, $\exp(-2\pi i f(t-t'))$, pertaining to stationarity. The other terms which pertain to initial phases obtained in the lower limit of the redshift integral (4) vanishes after time integration.

One implication of the transfer functions is that different frequency bins, $j \neq k$, are correlated, although very weakly. By following the same steps, it can be shown that the transfer function for $\langle\alpha_{aj}\beta_{bk}\rangle$ exactly vanishes. Thus, the α- and β-Fourier bins of Eq. (1) are uncorrelated. We leave it as a quick exercise to compute the transfer functions for $\langle\alpha_{a0}\alpha_{b0}\rangle$, $\langle\alpha_{a0}\alpha_{bk}\rangle$, and $\langle\alpha_{a0}\beta_{bk}\rangle$; the results are given by

$$\begin{aligned}\mathcal{C}^{0}(f) = [&4\sin(\pi f T)\sin(\pi {\rm FP}[fT])\cos(\pi {\rm IP}[fT]) \\ &+ 4\pi f T[\pi f T - \sin(2\pi f T)]]/(\pi^2 f^2 T^2), \end{aligned} \quad (24)$$

$$\mathcal{C}^{\alpha 0}_{k}(f) = -\frac{4k\sin^2(\pi f T)}{\pi(k^2 - f^2 T^2)}, \quad (25)$$

$$\mathcal{C}^{\beta 0}_{k}(f) = \frac{2[\pi f T \sin(2\pi f T) + \cos(2\pi f T) - 1]}{\pi^2(k^2 - f^2 T^2)}, \quad (26)$$

respectively, where ${\rm IP}[x]$ and ${\rm FP}[x]$ are symbolic representations of the integer and fractional parts of a real-valued input x, such that ${\rm IP}[x] + {\rm FP}[x] = x$. Representative transfer functions are shown in Fig. 1.

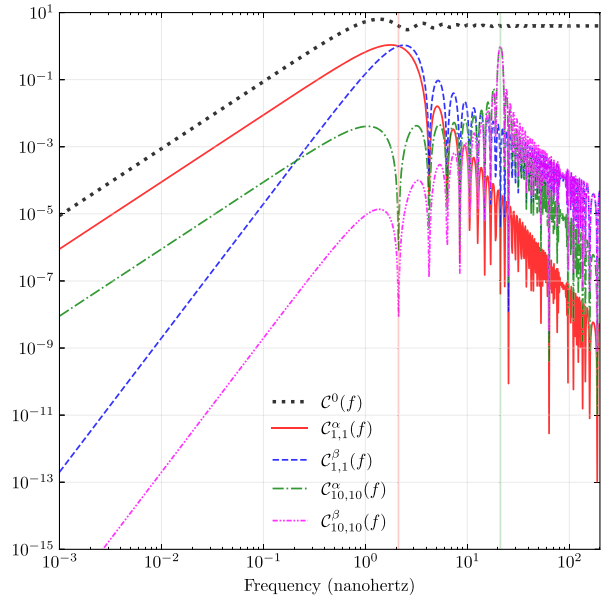
We will refer to Eqs. (22)–(26) as an α-, β-, DC, α-DC, and β-DC transfer functions, respectively.

[6]Another way this can be written is

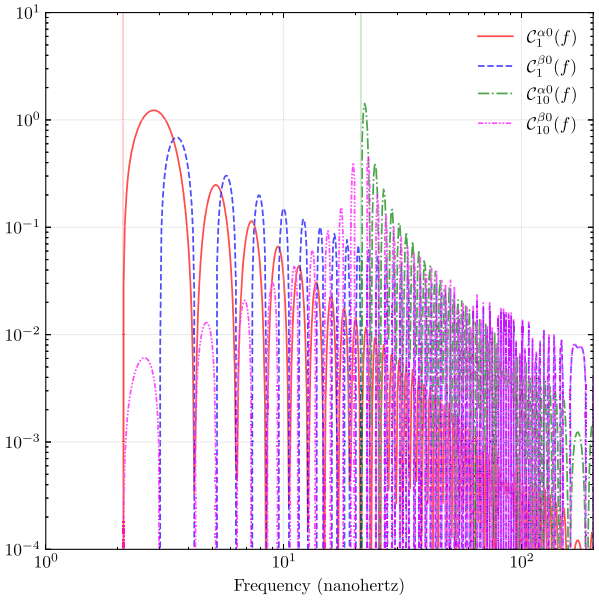
$$\mathcal{C}^{\alpha}_{j,k}(f) = \frac{4(-1)^{j+k} f_j f_k}{(f+f_j)(f+f_k)} {\rm sinc}(\pi T(f-f_j)){\rm sinc}(\pi T(f-f_k)),$$

$$\mathcal{C}^{\beta}_{j,k}(f) = \frac{4(-1)^{j+k} f^2}{(f+f_j)(f+f_k)} {\rm sinc}(\pi T(f-f_j)){\rm sinc}(\pi T(f-f_k)),$$

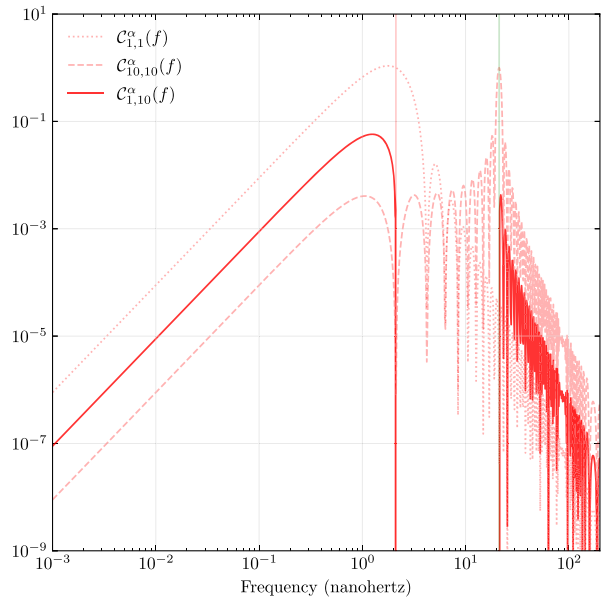
where ${\rm sinc}(x) = \sin(x)/x$. Note that $(-1)^k \sin(\pi f T)/(\pi T(f-f_k)) = {\rm sinc}(\pi T(f-f_k))$. This form makes the equivalence between the trigonometric (sine and cosine) and the exponential Fourier representations of a stochastic process transparent. See Appendix A.



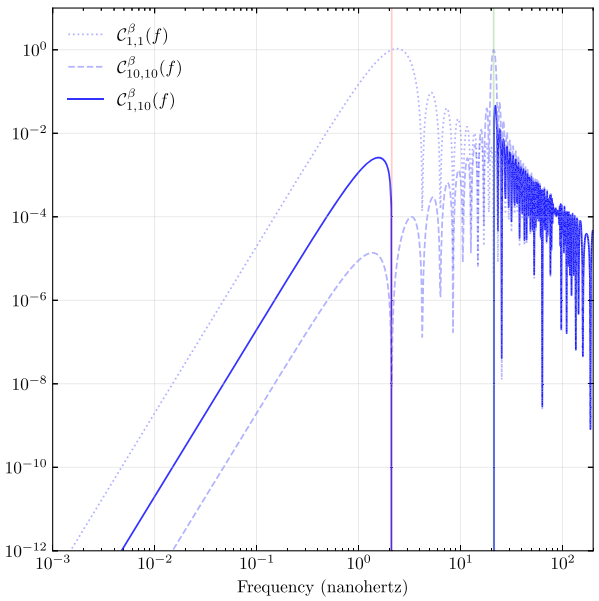
(a) α- and β-bin transfer functions (22-23) for $j = k$; and the DC transfer function (24)



(b) α-DC- and β-DC-bin transfer functions (25-26)



(c) α-bin transfer functions (22) for $j \neq k$



(d) β-bin transfer functions (23) for $j \neq k$

FIG. 1. Representative transfer functions (22)–(26) for an SGWB signal in PTA observation with $T = 15$ years, $f_1 \sim 2.1$ nanohertz, and $f_k \sim k f_1$.

Figure 1 shows that $\mathcal{C}^\alpha_{j,k}(f)$ and $\mathcal{C}^\beta_{j,k}(f)$ accommodate more low- and high-frequency components, respectively, relative to each other.[7] Mainly, it can be seen that the α-transfer function accepts more low-frequency contributions to the bins (shown are the 1st and 10th ones), compared with the corresponding β-transfer function which accepts more high-frequency contributions. This can be teased by the relation

$$\mathcal{C}^\beta_{j,k}(f) = \mathcal{C}^\alpha_{j,k}(f) f^2/(f_j f_k). \tag{27}$$

The shapes of the transfer functions are reminiscent of a mainlobe and sidelobes of a far-field radiation pattern [108]. Noticeably, the mainlobe carries the significant contribution; the sidelobes support subdominant contributions at all frequencies, except at integer multiples

[7]For this reason they were referred to as low pass and high pass filters in Refs. [117,132]. However, the $\mathcal{C}(f)$'s are not arbitrarily chosen as filters might misleadingly suggest.

of $1/T$ [108]. In addition, shown in Fig. 1(a) is the static or DC transfer function. We emphasize that the DC bin α_0 [see Eq. (1)] carries no frequency information, but is relevant when reconstructing nonprojected signal covariances with the right amplitudes. The transfer functions for $\langle\alpha_{a0}\alpha_{b0}\rangle$ [dotted-line in Fig. 1(a)], $\langle\alpha_{a0}\alpha_{bk}\rangle$, and $\langle\alpha_{a0}\beta_{bk}\rangle$ [Fig. 1(b)] were shown for completeness. It is also useful to look at the α- and β-bin transfer functions for different frequency components ($j \neq k$) [Fig. 1(c–d)]. This supports our previous statement that Fourier components of the correlation at different frequency bins are very weakly correlated. The transfer functions for different frequency bins $j \neq k$ are orders of magnitude lower compared to their $j = k$ counterparts, and are missing the significant power between the two frequency components, f_j and $f_k \neq f_j$. Consequently, the contributions of $\langle\alpha_{aj}\alpha_{bk}\rangle$ and $\langle\beta_{aj}\beta_{bk}\rangle$ with $j \neq k$ are subdominant compared to the $j = k$ contributions. Nonetheless, the off-diagonal terms' actual contribution can be quantified by an efficient reconstruction of the time-domain covariance (see Ref. [118]).

The transfer functions provide a unified formalism for computing the PTA correlation in each Fourier bin due to the SGWB signal. All the correlation components can now be expressed as

$$\langle X_{aj}Y_{bk}\rangle = \mathcal{F}[I(f)\gamma(fD_a, fD_b, \hat{e}_a, \hat{e}_b), \mathcal{C}^{(XY)}_{j,k}(f)], \tag{28}$$

where the functional $\mathcal{F}$ is given by

$$\mathcal{F}[G(f,y), \mathcal{C}(f)] = \int_{f_{\min}}^{f_{\max}} \frac{2df}{(2\pi f)^2} G(f,y)\mathcal{C}(f), \tag{29}$$

and $\mathcal{C}^{(XY)}_{jk}(f)$ are transfer functions given by Eqs. (22)–(26).

It is worth emphasizing that the components $\langle X_{aj}Y_{bk}\rangle$ are the frequency- and Fourier-domain representations of the stationary covariance function. In this regard, the timing residual correlation can be written in Fourier space as

$$\langle r(t,\hat{e}_a,)r(t',\hat{e}_b)\rangle = \sum_{jk}[\langle\alpha_{aj}\alpha_{bk}\rangle \sin(\omega_j t)\sin(\omega_k t') + \langle\beta_{aj}\beta_{bk}\rangle \cos(\omega_j t)\cos(\omega_k t')] + \cdots \tag{30}$$

where the ellipses are all terms correlated with the DC component, i.e.,

$$\frac{\langle\alpha_{a0}\alpha_{b0}\rangle}{4} + \frac{1}{2}\sum_k[\langle\alpha_{ak}\alpha_{b0}\rangle \sin(\omega_k t) + \langle\alpha_{bk}\alpha_{a0}\rangle \sin(\omega_k t') + \langle\beta_{ak}\alpha_{b0}\rangle \cos(\omega_k t) + \langle\beta_{bk}\alpha_{a0}\rangle \cos(\omega_k t')]. \tag{31}$$

This highlights that the main contributions due to the SGWB come from the Fourier components $\langle\alpha_{ak}\alpha_{bk}\rangle$ and $\langle\beta_{ak}\beta_{bk}\rangle$. Note that the variances of the sine- and cosine-Fourier coefficients are different, because the Fourier basis $\{\sin(2\pi kt/T), \cos(2\pi kt/T),\ \text{for } k \in \mathbb{N}\}$ does not diagonalize the covariance of a signal with a time scale that is much larger compared to the observation period (see Sec. VII for details). Turning this around, it is straightforward to show that if the signal's harmonic frequencies align with the observational frequencies (e.g., take a source with a power spectral density $\mathcal{S}(f) = \sum_k s_k\delta(f - k/T)$), then the covariance is going to be diagonalized and the variances of the sine- and cosine-Fourier coefficients are going to have the same probability distribution function. The decomposition (30)–(31) can also be taken as the Green's function expansion in a Fourier basis with a finite time window.[8]

Mathematically, the relation between the variances can be teased out using (27). The windowing of a stationary signal can also be used to physically argue why the variances of the sine and cosine coefficients will be different. Sines and cosines differ by fixed phases. However, in a stationary signal, sine and cosine modes have equal probability distribution functions (and hence moments, including the variance), because the fixed phase difference should not be distinguishable under stationarity. The outcome of an observation however can be strikingly different when only a short train of the signal is measured. In this case, the short period of observation or windowing breaks stationarity, and as a consequence distinguishes sines and cosines by their fixed phases.

It might be useful to note that the lower limit of (4) implies that the DC and non-DC coefficients are related mathematically; it can be shown that $\alpha_{a0}/2 = -\sum_{k>=1}\beta_{ak}$, $\langle\alpha_{a0}\alpha_{b0}\rangle/4 = \sum_{jk}\langle\beta_{aj}\beta_{bk}\rangle$, and $0 = \langle\alpha_{a0}\alpha_{b0}\rangle/2 + \sum_k(\langle\beta_{ak}\alpha_{b0}\rangle + \langle\beta_{bk}\alpha_{a0}\rangle)/2 + \sum_{jk}\langle\beta_{aj}\beta_{bk}\rangle$. The same arbitrary lower limit produces the extra phase terms in the

[8]We elaborate on diagonalization. A stationary random process $y(t)$ can be represented as $y(t) = \sum_k \tilde{y}_k\phi_k(t)$ using a complete set of orthogonal basis functions $\{\phi_k(t)\}$. In this representation, the covariance $\langle y(t)y(t')\rangle$ can be shown to be $\langle y(t)y(t')\rangle = \sum_k\langle\tilde{y}_k^2\rangle\phi_k(t)\phi_k(t') + \sum_{j\neq k}\langle\tilde{y}_j\tilde{y}_k\rangle\phi_j(t)\phi_k(t')$, which is broken down into diagonal ($j = k$) and off-diagonal ($j \neq k$) contributions; the quantities $\langle\tilde{y}_j\tilde{y}_k\rangle$ represent $\langle y(t)y(t')\rangle$ in this basis. The Wiener-Khinchin theorem reveals that there is a preferred set of basis functions $\{\phi^\star_k(t)\} \equiv \{\sin(2\pi kt/T_s), \cos(2\pi kt/T_s)\}$ (which happens to be a Fourier basis) that diagonalizes the covariance as

$$\langle y(t)y(t')\rangle \overset{\phi=\phi^\star}{\to} \sum_k \langle\tilde{y}_k^2\rangle\phi^\star_k(t)\phi^\star_k(t'),$$

or $\langle\tilde{y}_j\tilde{y}_k\rangle = 0$ for $j \neq k$. T_s is a time scale, such that a stationary signal's harmonic frequencies are separated by T_s^{-1}. An important point is that in the *preferred* basis, the variance of the sine and cosine pairs in each frequency bin are equal, and that different frequency bins are completely uncorrelated. Because of this preferentiality, there is no reason to expect that the same outcome will be realized in any arbitrary basis, such as in a Fourier basis with a different time window.

temporal correlation (12), whereas only the stationary term, i.e., $\exp(-2\pi f(t-t'))$, is physical. See also Appendix A of [140] for a related discussion.

IV. COMPARISON WITH SIMULATION

We motivate the results—Eqs. (28)–(29) and Eqs. (22)–(26)—by comparing with simulations, based on GWs emitted by a finite number of binaries. We use the standard TEMPO2 [126,141,142] pulsar timing software and its python wrapper LIBSTEMPO to simulate a clean SGWB signal (noise-free); we choose $A_{\rm gw} = 10^{-15}$, $\gamma_{\rm gw} = 13/3$, and $n_{\rm bhb} = 10^3$ for the SGWB characteristic stain, spectral index, and number of sources/SMBHBs, respectively. In addition, we take the GW emission frequencies to be $f \in (1, 100)$ nHz. For the reference positions on the sphere, we refer to the NANOGrav 15-year dataset's 67 millisecond pulsars.

In addition, we employ our own simulation of a Gaussian SGWB signal in a PTA; which we refer to as PTAfast in the labels; building on a software that we developed for deriving correlation functions for PTA.[9] This was done by first generating a set of pulsar positions on the celestial sphere, $\hat{e}_a$, for $a = 1, 2, \ldots n_{\rm psrs}$ pulsars; we generate $n_{\rm psrs} = 100$ pulsars and scatter them across the sphere. Then, for each pulsar, labeled a, we generate a set of Fourier coefficients, α_{ak} and β_{ak}, for $k = 1, 2, \ldots k_{\rm max}$ frequency bins, where $k_{\rm max}$ is determined by the highest frequency of the signal. To generate the signal contribution, for each frequency bin, we draw independent random numbers, ξ, from a Gaussian distribution with zero mean and unit variance. We correlate the pulsars according to Eqs. (28)–(29) and Eqs. (22)–(26) by constructing the covariance matrix $\mathbf{\Sigma}$, given by

$$\Sigma^k_{ab} \equiv \begin{pmatrix} \langle \alpha_{ak}\alpha_{bk}\rangle & 0 \\ 0 & \langle \beta_{ak}\beta_{bk}\rangle \end{pmatrix}, \tag{32}$$

for all pulsar pairs (a, b) and frequency bins k. Note that for a fixed frequency bin k, the covariance matrix $\mathbf{\Sigma}$ is a $2n_{\rm psrs} \times 2n_{\rm psrs}$ matrix, with the diagonal elements given by the variances of the Fourier coefficients. The off-diagonal elements in the upper left and lower right block matrices, $\langle \alpha_{ak}\alpha_{bk}\rangle$ and $\langle \beta_{ak}\beta_{bk}\rangle$, factor in pulsar pair correlations (HD curve). The rest of the off-diagonal elements vanish because the α- and β-Fourier coefficients are uncorrelated. The Fourier components $\langle \alpha_{ak}\alpha_{bk}\rangle$ and $\langle \beta_{ak}\beta_{bk}\rangle$ are computed by convolving the transfer functions (22)–(26) with a power-law power spectral density,

$$S(f) \equiv \frac{A^2_{\rm gw}}{12\pi^2}\left(\frac{f}{f_{\rm yr}}\right)^{-\gamma_{\rm gw}} f^{-3}_{\rm yr}, \tag{33}$$

over the frequency range of the SGWB signal, $f \in (1, 100)$ nHz; $f_{\rm yr} = {\rm yr}^{-1}$. The coefficients α_{ak} and β_{ak} are then obtained by applying the Cholesky decomposition to the covariance matrix $\mathbf{\Sigma} \equiv \mathbf{L}\mathbf{L}^{\rm T}$ and multiplying the lower triangular matrix $\mathbf{L}$ to the vector $\boldsymbol{\xi}$, i.e., $\alpha, \beta \sim \mathbf{L}\boldsymbol{\xi}$ [130]. The resulting Fourier coefficients are used to simulate the timing residuals via Eq. (1), i.e., $r(t, \hat{e}_a) \equiv \sum_k [\alpha_{ak}\sin(\omega_k t) + \beta_{ak}\cos(\omega_k t)]$. A sample of correlated residuals simulated by accounting for transfer functions are shown in Fig. 2. Timing residual simulations generated with and without transfer functions are visually distinguishable. Time correlated signals can be easily generated in the time-domain using Gaussian processes given the corresponding covariance matrix. The resulting time series for any signal with a continuous support exhibits all frequency components. In the frequency-domain, these frequency components are accounted for by transfer functions. We refer the interested reader to Appendix C for more details.

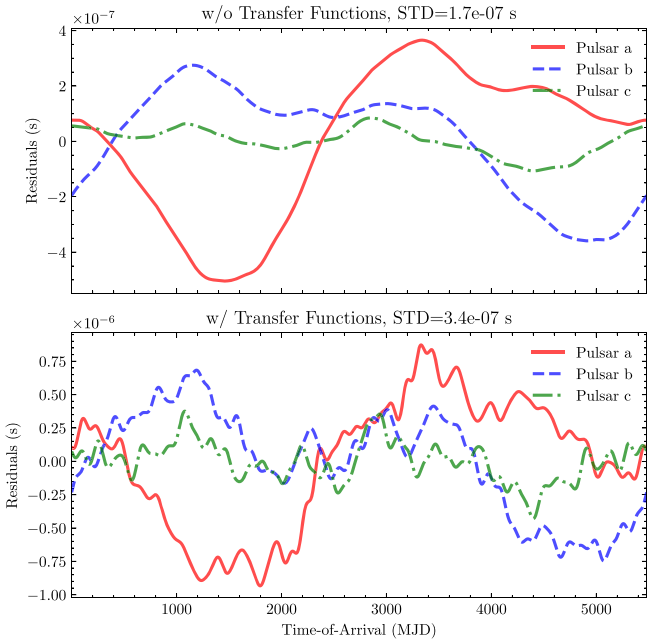
With either TEMPO2 or PTAfast PTA simulations, we process the timing data as follows. Each PTA realization gives a time series[10]: $r(t, \hat{e}_a)$, for $a = 1, 2, \ldots n_{\rm psrs}$ pulsars. The Fourier coefficients α_{ak}, β_{ak}, for each pulsar, are extracted via a standard discrete Fourier transform routine, i.e., discretized Eq. (2). This function is available in many scientific computing libraries such as SCIPY. Once the Fourier coefficients are available, for each frequency bin (index k), products of α_{ak} and β_{bk} are binned spatially (based on the pulsar-pair angular separation $\hat{e}_a \cdot \hat{e}_b$). This leads to a set

$$\{\alpha_{ak}\alpha_{bk}, \beta_{ak}\beta_{bk}, \alpha_{ak}\beta_{bk}; k = 1, \ldots, n_{\rm bins}; (a, b) \equiv \text{all pulsar pairs}\}. \tag{34}$$

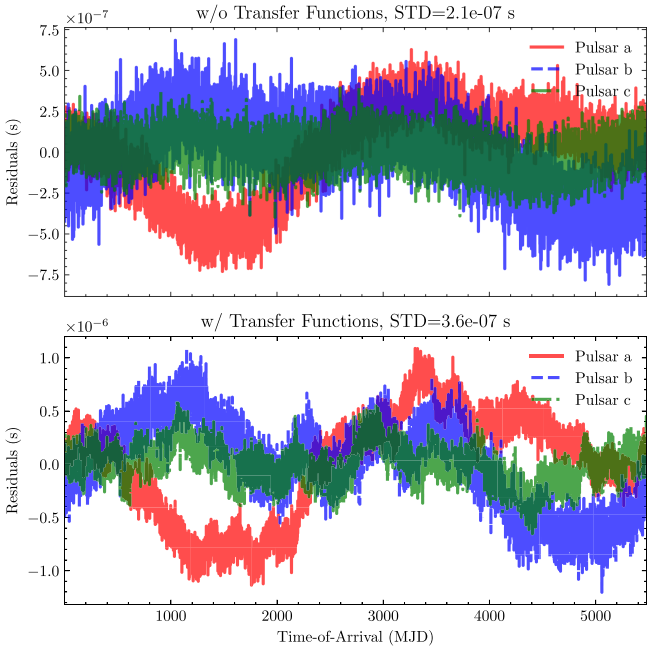
The sample averages are computed over each set (34), fixed k and fixed angular bin $\hat{e}_a \cdot \hat{e}_b \pm \Delta(\hat{e}_a \cdot \hat{e}_b)$ where $\Delta(\hat{e}_a \cdot \hat{e}_b)$ is an angular bin width, e.g., $\Delta(\hat{e}_a \cdot \hat{e}_b) \sim \cos(12°)$ if we take 15 angular bins ($a \neq b$). We associate the terms $a = b$ (autocorrelation) with a zeroth angular bin at $\zeta = 0$. The processing of one PTA realization ends when the sample statistics are computed in all frequency and angular bins. For our tests, we consider 14 frequency bins, centered at $f_k = k/T$ for $k = 1, \ldots, 15$, and 16 angular bins, centered at $\zeta_q = q \times (180°/15)$ for $q = 0, \ldots, 15$. Then, the entire process is repeated numerous times with the same input; each realization turns in sample statistics in a PTA realization, representative of an underlying ensemble probability distribution function (PDF) across realizations.

[9] This foreshadows a version of our open-source code PTAfast [143] equipped with pulsar timing residual simulations.

[10] In general, each PTA realization will have signal and noise. If the noise has only a white component, then our results will hold in the first few frequency bins. On the other hand, if there are other correlated noises (a red process) in the data, a full PTA analysis can be done to distinguish the correlated components from the spatially correlated GWB signal.



(a) signal



(b) signal + white noise

FIG. 2. Simulated pulsar timing residuals due to a Gaussian SGWB signal with a power-law spectrum (33); signal parameters: $A_{\rm gw} = 10^{-15}$, $\gamma_{\rm gw} = 13/3$, and $f_{\rm gw} \in (1, 100)$ nHz. Transfer functions (22)-(23) are implemented in PTAfast. The STD shown are the average standard deviations of the timing residuals of the pulsar sample $\{a, b, c\}$; STD $= \{\sqrt{E[r(t)^2] - E[r(t)]^2}\} \propto$ Amplitude of the time series, where E is a time average operator and $\{\cdots\}$ is the sample average over a, b, c. Note that $E[r(t)] = 0$ or that $\alpha_0 = 0$ in all cases.

The resulting sample averages and two-point correlation function with $\mathcal{O}(10^3)$ realizations are shown in green (TEMPO2) and red (PTAfast) points with error bars in Fig. 3. This is shown together with Gaussian theoretical expectation values (black points and curves) obtained using the formalism (28)–(29) and the transfer functions (22)–(23). We refer to $\{\alpha_k\beta_k\}/\sqrt{\{\alpha_k^2\}\{\beta_k^2\}}$ and $\{\alpha_{ak}\beta_{bk}\}$ as a cross-Fourier statistic and a cross-Fourier spatial correlation, respectively.

The result shows that both TEMPO2 and PTAfast simulations are in agreement with the theoretical predictions. The variances of the α- and β-Fourier coefficients diverge in frequency space. This is because the Fourier basis over the observational frequencies $f_k = k/T$, i.e., $\{\sin(2\pi kt/T), \cos(2\pi kt/T)\}$, does not diagonalize the signal covariance that has a characteristic time scale much larger than the observational window. The transfer functions (22)–(23) account for the fact that the signal is only observed in a very short window compared to the signal time scale. The two-point correlation function is consistent with the HD correlation, indicating a GW observation. The cross-Fourier statistic $\sim\{\alpha_k\beta_k\}$ and the cross-Fourier spatial correlation $\{\alpha_{a1}\beta_{b1}\}$ are consistent with their Gaussian expectation values at zero. Both vanish theoretically for all frequency and angular bins since the transfer function between α- and β-Fourier coefficients is zero. (This is a useful reference point for processes that correlate the sine- and cosine-Fourier coefficients across pulsar pairs, such as circular polarization.)

To evaluate the theoretical expectation values, we consider a SMBHB power spectral density (33) with a characteristic strain amplitude of $A_{\rm gw} = 10^{-15}$ and a spectral index of $\gamma_{\rm gw} = 13/3$. When evaluating the integrals, we truncate the lower and upper limits to the input signals's frequencies; so $f_{\rm min} = 1$ nHz and $f_{\rm max} = 100$ nHz. The integrations are performed in log-space in frequency.

It is worth highlighting that the theoretical Gaussian model shown in Fig. 3 (black points and curves) is described by a single parameter, $A_{\rm gw}$; the spectral index is fixed to $\gamma_{\rm gw} = 13/3$ for circular SMBHBs. Furthermore, the choice of reference frequency, $f_{\rm ref} = f_{\rm yr}$, is arbitrary; changing the reference frequency, $f_{\rm ref} \to f'_{\rm ref}$, amounts to shifting the amplitude by $A_{\rm gw} \to A'_{\rm gw} = A_{\rm gw}(f'_{\rm ref}/f_{\rm ref})^{-13/3}$. For a power law power spectrum (33), the appropriate shift will be $A_{\rm gw} \to A'_{\rm gw} = A_{\rm gw}(f'_{\rm ref}/f_{\rm ref})^{-\gamma_{\rm gw}}$. In practice, shifting the reference frequency is going to statistically change the covariance between $A_{\rm gw}$ and $\gamma_{\rm ref}$, especially when errors are huge. However, if the SGWB signal were interpreted with a diagonal basis utilizing Fourier modes at frequencies $f_k = k/T$, then the choice of reference frequency could turn to be a source of a systematic error on the measured amplitude of the SGWB. See [117,118] for related

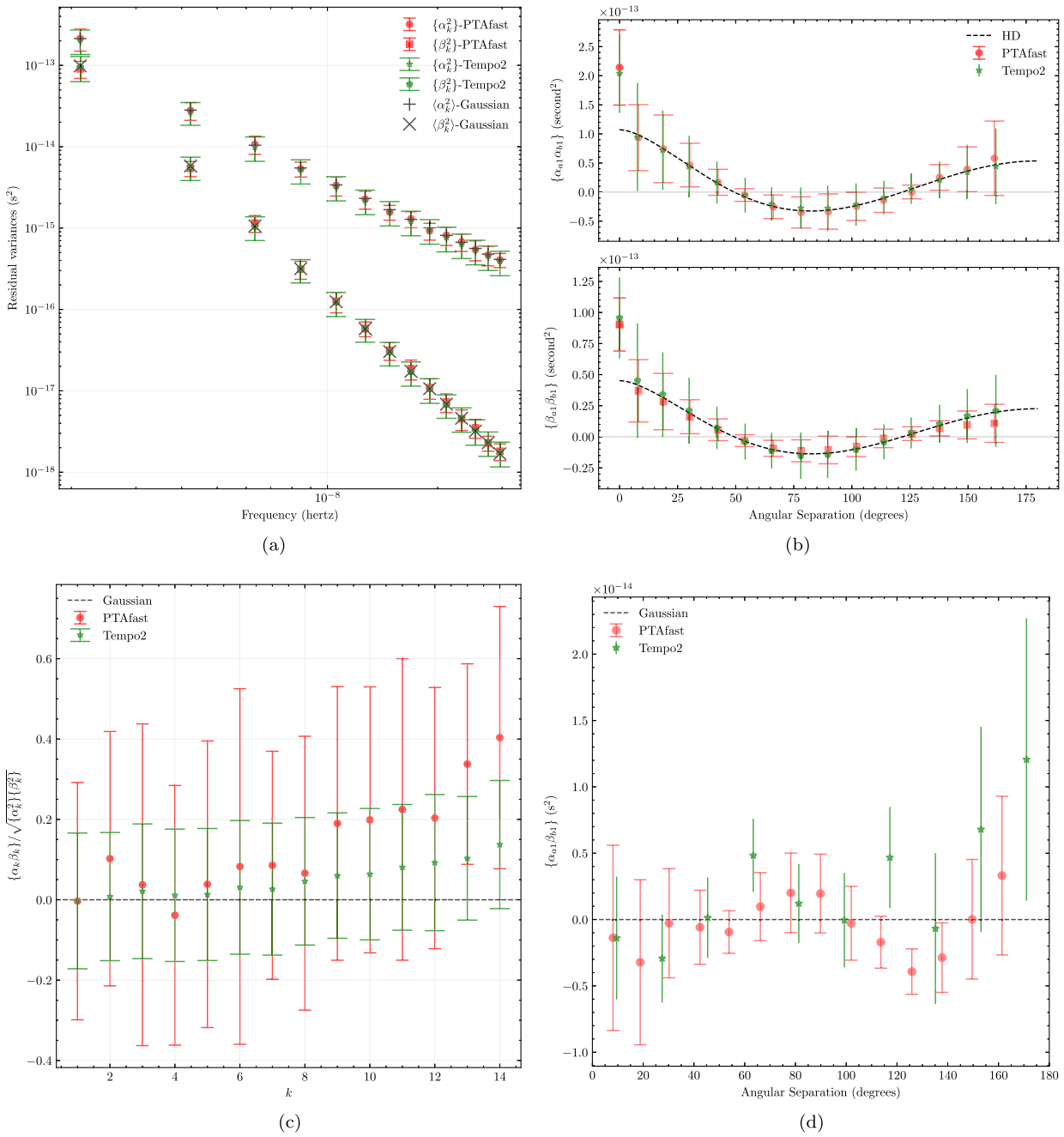


FIG. 3. Fourier components of the timing residual correlation: (a) sample variances, (b) two-point correlation function, (c) cross-Fourier statistic $\{\alpha_k\beta_k\}/\sqrt{\{\alpha_k^2\}\{\beta_k^2\}}$, and (d) cross-Fourier spatial correlation $\{\alpha_{a1}\beta_{b1}\}$. Green and red points refer to TEMPO2 (67 pulsars at NG positions [1]) and PTAfast (100 pulsars scattered anisotropically) simulations, respectively, and the error bars in subplots (a–c) represent the standard error across $\mathcal{O}(10^3)$ realizations. For subplot (d) the error bars shown are the error on the mean. Black points and dashed curves show the Gaussian theoretical expectation values based on Eqs. (28)–(29) and Eqs. (22)–(26) such as the HD curve in (b).

systematic errors rooted in approximating the covariance with only diagonal terms and infinitesimally narrow filters.

In PTA analyses, the raw time-of-arrival data undergoes postfitting; effectively projecting out constant, linear, and quadratic terms in the time series. This reduces the power difference between the (α- and β-) frequency bins and suppresses subnanohertz GW contributions. The resulting observation can be characterized by a transmission function which must be convolved with the power spectrum. Crucially, our results indicate that the distinction of the α- and β-variances persists regardless of postfitting, reinforcing the necessity of revisiting signal modeling

assumptions. While real PTA data is also subject to contamination from white noise, particularly at higher frequency bins, and intrinsic red noise in each pulsar, these factors primarily affect the precision of SGWB measurements. White noise diminishes the experimental sensitivity at high frequencies, while red noise contributes to the overall measurement uncertainty.

We emphasize that we do not use the variances as direct estimators of the power spectral density, e.g., by constructing the periodogram. Instead, we compute the full covariance function in the frequency- and Fourier-domain, evaluating integrals of the form (29) to properly account for the dominant frequency correlations [108,118].

The reference pulsar positions are arbitrary; for example, using Meerkat PTA positions [144,145] would yield similar results, with differences manifesting only in the ensemble variance. However, the number of pulsars in the array plays a crucial role in determining the statistical variance across realizations—larger arrays provide better sampling and reduce the impact of statistical fluctuations (see Appendix D for details).

The choices for the number of frequency and angular bins are also somewhat arbitrary, but are constrained by practical considerations such as the number of pulsars and the cadence of the timing data. In particular, resolving higher frequency bins requires sufficiently dense sampling; for instance, in Fig. 3, the apparent systematic increase in the cross-Fourier statistic at high frequencies for both TEMPO2 and PTAfast is attributable to limitations in cadence; $\mathcal{O}(10^4)$ time-of-arrivals over 15 years were needed to resolve these bins. These considerations highlight the importance of array size and data quality, but do not affect the agreement between simulation and theory, underscoring the robustness of the analysis.

V. THE POLARIZED SIGNAL: SIMULATING CIRCULAR POLARIZATION IN A PTA

We lay down the formalism extending Sec. III to include the signal imprinted by a circularly polarized SGWB on the PTA residuals.

A. Circularly polarized basis tensors and stokes parameters

We consider a Gaussian SGWB with a two-point function of the generalized form,

$$\langle h_A(f,\hat{k}) h^*_{A'}(f',\hat{k}')\rangle = \delta(f-f')\delta(\hat{k}-\hat{k}')P_{AA'}(f,\hat{k}), \quad (35)$$

where the power spectra, $P_{AA'}(f,\hat{k})$, is now anisotropic (direction-dependent); in contrast with Eq. (9). Then, the unpolarized signal can be described in the limit $P_{AA'}(f,\hat{k}) \to I(f)\delta_{AA'}$ (Secs. III–IV).

Analogous to electromagnetic waves, a suitable way to look into circular polarization is through Stokes parameters. To do so, we consider complex circular polarization basis tensors; defined as

$$\varepsilon_R = \frac{(\varepsilon_+ + i\varepsilon_\times)}{\sqrt{2}}, \qquad \varepsilon_L = \frac{(\varepsilon_+ - i\varepsilon_\times)}{\sqrt{2}}, \quad (36)$$

where ε_R (ε_L) stands for a right-handed (left-handed) GW with a positive (negative) helicity. The GW amplitudes in Eq. (3) in the two different bases are related to each other via

$$h_R = \frac{(h_+ - ih_\times)}{\sqrt{2}}, \qquad h_L = \frac{(h_+ + ih_\times)}{\sqrt{2}}. \quad (37)$$

Then, the power spectra or coherency matrix $P_{AA'}(f,\hat{k})$ in Eq. (35) can be associated with Stokes parameters, I, Q, U, and V via

$$\begin{aligned} I &= [\langle h_R h^*_R\rangle + \langle h_L h^*_L\rangle]/2, \\ Q + iU &= \langle h_L h^*_R\rangle, \\ Q - iU &= \langle h_R h^*_L\rangle, \\ V &= [\langle h_R h^*_R\rangle - \langle h_L h^*_L\rangle]/2, \end{aligned} \quad (38)$$

which are functions of the frequency f and the propagation direction $\hat{k}$. The $I(f,\hat{k})$ is the intensity, $Q(f,\hat{k})$ and $U(f,\hat{k})$ represent the linear polarization, and $V(f,\hat{k})$ is the circular polarization. In terms of the Stokes parameters, an unpolarized signal is characterized by $I \neq 0$ and $Q = U = V = 0$. A circularly polarized signal is characterized by $I \neq 0$ and $V \neq 0$, while $Q = U = 0$.

Now, we consider a circularly polarized SGWB. We expand the Stokes parameters in terms of spherical harmonics as

$$\begin{aligned} I(f,\hat{k}) &= \sum_{\ell m} I_{\ell m}(f) Y_{\ell m}(\hat{k}), \\ V(f,\hat{k}) &= \sum_{\ell m} V_{\ell m}(f) Y_{\ell m}(\hat{k}), \end{aligned} \quad (39)$$

where $I(-f,\hat{k}) = I(f,\hat{k})$ and $V(-f,\hat{k}) = -V(f,\hat{k})$. Since $I(f,\hat{k})$ and $V(f,\hat{k})$ are real, we have

$$\begin{aligned} I^*_{\ell m}(f) &= (-1)^m I_{\ell -m}(f), \\ V^*_{\ell m}(f) &= (-1)^m V_{\ell -m}(f). \end{aligned} \quad (40)$$

B. Timing residual power spectrum and correlation

Following Secs. III A–III B with the two-point function (35), the timing residual power spectrum can be shown to be [100]

$$\langle a_{\ell_1 m_1} a^*_{\ell_2 m_2}\rangle = \int_{-\infty}^{\infty} \frac{df}{(2\pi f)^2} C(f,t_a,t_b) \times \sum_{X=\{I,V\}} \sum_{\ell m} X_{\ell m}(f) \tilde{\gamma}^X_{\ell m,\ell_1 m_1 \ell_2 m_2}(fD_a,fD_b), \quad (41)$$

where the coefficients are given by a time integral and Wigner-3j symbols

$$\tilde{\gamma}^{I,V}_{\ell m,\ell_1 m_1 \ell_2 m_2}(fD_a,fD_b) = (-1)^{m_1}[1\pm(-1)^{\ell+\ell_1+\ell_2}] J_{\ell_1}(fD_a) J^*_{\ell_2}(fD_b) \times \sqrt{\frac{(2\ell+1)(2\ell_1+1)(2\ell_2+1)}{4\pi}} \times \begin{pmatrix} \ell & \ell_1 & \ell_2 \\ 0 & -2 & 2 \end{pmatrix} \begin{pmatrix} \ell & \ell_1 & \ell_2 \\ m & -m_1 & m_2 \end{pmatrix}. \quad (42)$$

The $J_\ell(y)$'s are defined as

$$J_\ell(y) = \sqrt{2}\pi i^\ell \sqrt{\frac{(\ell+2)!}{(\ell-2)!}} \int_0^{2\pi y} dx e^{ix} \frac{j_\ell(x)}{x^2}, \quad (43)$$

and the time kernel $C(f,t,t')$ is given by Eq. (12). Then, the pulsar timing residual correlation can be expressed in the form

$$\langle r(t_a,\hat{e}_a) r(t_b,\hat{e}_b)\rangle = \int_{-\infty}^{\infty} \frac{df}{(2\pi f)^2} C(f,t_a,t_b) \times \sum_{X=\{I,V\}} \sum_{\ell m} X_{\ell m}(f) \gamma^X_{\ell m}(fD_a,fD_b;\hat{e}_a,\hat{e}_b). \quad (44)$$

where the ORFs $\gamma^{I,V}_{\ell m}(fD_a,fD_b;\hat{e}_a,\hat{e}_b)$ are defined as

$$\gamma^{I,V}_{\ell m}(fD_a,fD_b;\hat{e}_a,\hat{e}_b) = \sum_{\ell_1 m_1 \ell_2 m_2} \tilde{\gamma}^{I,V}_{\ell m,\ell_1 m_1 \ell_2 m_2}(fD_a,fD_b) Y_{\ell_1 m_1}(\hat{e}_a) Y^*_{\ell_2 m_2}(\hat{e}_b). \quad (45)$$

Note that the ORFs are complex in general. As a special case, γ^I_{00} is real for $D_a = D_b$ and $\gamma^V_{00} = 0$. The latter is expected for a circularly polarized SGWB because of the parity symmetry in a PTA experiment. Under the limit that $fD_a \gg 1$ and $fD_b \gg 1$, γ^I_{00} reduces to the HD curve and $\tilde{\gamma}^{I,V}_{\ell m,\ell_1 m_1 \ell_2 m_2}(fD_a,fD_b)$ becomes constant real values. Since $\gamma^V_{00} = 0$, a PTA experiment is insensitive to the circular polarization of an isotropic circularly polarized SGWB. Some degree of anisotropy in the SGWB is needed for circular polarization to be detectable [128].

C. Correlation in the computational frame

In the computational frame [100,127–129,131], in which pulsar a is placed along the $\hat{\mathbf{z}}$-axis while pulsar b is in the $\hat{\mathbf{x}}-\hat{\mathbf{z}}$ plane, the timing-residual correlation becomes

$$\langle r(t_a,\hat{e}_a) r(t_b,\hat{e}_b)\rangle = \int_{-\infty}^{\infty} \frac{df}{(2\pi f)^2} C(f,t_a,t_b) \times \sum_{X=\{I,V\}} \sum_{\ell m} X_{\ell m}(f) \gamma^X_{\ell m}(fD_a,fD_b,\zeta), \quad (46)$$

where ζ is their separation angle ($\cos\zeta = \hat{e}_a \cdot \hat{e}_b$) and

$$\gamma^{I,V}_{\ell m}(fD_a,fD_b,\zeta) = \sum_{\ell_1 \ell_2} (-1)^m \frac{2\ell_1+1}{4\pi} [1\pm(-1)^{\ell+\ell_1+\ell_2}] J_{\ell_1}(fD_a) J^*_{\ell_2}(fD_b) Y_{\ell_2 m}(\zeta,0) \sqrt{(2\ell+1)(2\ell_2+1)} \times \begin{pmatrix} \ell & \ell_1 & \ell_2 \\ 0 & -2 & 2 \end{pmatrix} \begin{pmatrix} \ell & \ell_1 & \ell_2 \\ m & 0 & -m \end{pmatrix}. \quad (47)$$

The reflection property (B9) guarantees that the ORFs in the computational frame have the conjugate relations

$$\gamma^I_{\ell -m} = (-1)^m \gamma^I_{\ell m}, \quad (48)$$

$$\gamma^V_{\ell -m} = (-1)^{m+1} \gamma^V_{\ell m}. \quad (49)$$

Then, using Eqs. (40) and (49), we can recast the sum in Eq. (46) into

$$\sum_{X=\{I,V\}} \sum_{\ell m} X_{\ell m}(f) \gamma^X_{\ell m}(fD_a,fD_b,\zeta) = \sum_{\ell m} [\mathrm{Re}[I_{\ell m}(f)] \gamma^I_{\ell m}(fD_a,fD_b,\zeta) + i\,\mathrm{Im}[V_{\ell m}(f)] \gamma^V_{\ell m}(fD_a,fD_b,\zeta)]. \quad (50)$$

Finally, the timing residual correlation in the computational frame can be expressed as

$$\langle r(t_a,\hat{e}_a)r(t_b,\hat{e}_b)\rangle = \int_0^\infty \frac{df}{(2\pi f)^2}\Big\{C(f,t_a,t_b)\sum_{\ell m}[I_{\ell m}(f)\gamma^I_{\ell m}(fD_a,fD_b,\zeta)+V_{\ell m}(f)\gamma^V_{\ell m}(fD_a,fD_b,\zeta)] + C(f,t_a,t_b)^*\sum_{\ell m}[I_{\ell m}(f)\gamma^{I*}_{\ell m}(fD_a,fD_b,\zeta)-V_{\ell m}(f)\gamma^{V*}_{\ell m}(fD_a,fD_b,\zeta)]\Big\}. \quad (51)$$

To arrive at the last expression, we used $J_\ell(-fD)=-J^*_\ell(fD)$. In the case $fD_a \gg 1$ and $fD_b \gg 1$, $\gamma^{I,V}_{\ell m}(fD_a,fD_b,\zeta)$ become real functions [100].[11] In general, with $t_a \neq t_b$, the pulsar timing residual correlation can be expressed as

$$\langle r(t_a,\hat{e}_a)r(t_b,\hat{e}_b)\rangle = \int_0^\infty \frac{2df}{(2\pi f)^2}\Big[\mathrm{Re}[C(f,t_a,t_b)]\sum_{\ell m} I_{\ell m}(f)\gamma^I_{\ell m}(fD_a,fD_b,\zeta) + \mathrm{Im}[C(f,t_a,t_b)]\sum_{\ell m} iV_{\ell m}(f)\gamma^V_{\ell m}(fD_a,fD_b,\zeta)\Big], \quad (53)$$

where

$$\mathrm{Re}[C(f,t_a,t_b)] = 1-\cos(2\pi f t_a)-\cos(2\pi f t_b)+\cos[2\pi f(t_b-t_a)],$$
$$\mathrm{Im}[C(f,t_a,t_b)] = \sin(2\pi f t_a)-\sin(2\pi f t_b)+\sin[2\pi f(t_b-t_a)]. \quad (54)$$

The time kernels $\mathrm{Re}[C(f,t_a,t_b)]$ and $\mathrm{Im}[C(f,t_a,t_b)]$ are owed to wave propagation in time and are the generalization of Eq. (12) to a circularly polarized SGWB.

For visualization, assume that I_{lm}'s, V_{lm}'s, and their corresponding ORFs weakly depend on frequency over the PTA sensitivity range, and that $fD_a, fD_b \gg 1$ is satisfied for all pulsar pairs. Then, we have

$$\langle r(t_a,\hat{e}_a)r(t_b,\hat{e}_b)\rangle = \bar{C}(t_a,t_b)\sum_{\ell m} I_{\ell m}\gamma^I_{\ell m}(\zeta) + \bar{S}(t_a,t_b)\sum_{\ell m} iV_{\ell m}\gamma^V_{\ell m}(\zeta), \quad (55)$$

where the weighted temporal correlations $\bar{C}(t_a,t_b)$ and $\bar{S}(t_a,t_b)$ are defined as $n_\delta\int_{1/T}(2df/(2\pi f)^2)\mathrm{Re}[C(f,t_a,t_b)]$ and $n_\delta\int_{1/T}(2df/(2\pi f)^2)\,\mathrm{Im}[C(f,t_a,t_b)]$. The normalization constant $n_\delta = 1/\int_{1/T}(2df/(2\pi f)^2)$ is arbitrary and was chosen for illustration purposes. The integrals were regularized by using an infrared cutoff at $f\sim 1/T$. Figure 4 shows $\bar{C}(t_a,t_b)$ and $\bar{S}(t_a,t_b)$ as a function of time and the spatial correlations $\gamma^I_{00}(\zeta)=\gamma^{\mathrm{HD}}(\zeta)$, $\gamma^I_{10}(\zeta)$, $\gamma^I_{11}(\zeta)$, and $\gamma^V_{11}(\zeta)$.

[11] As a special case, when $t_a = t_b = t$, the pulsar timing residual correlation becomes

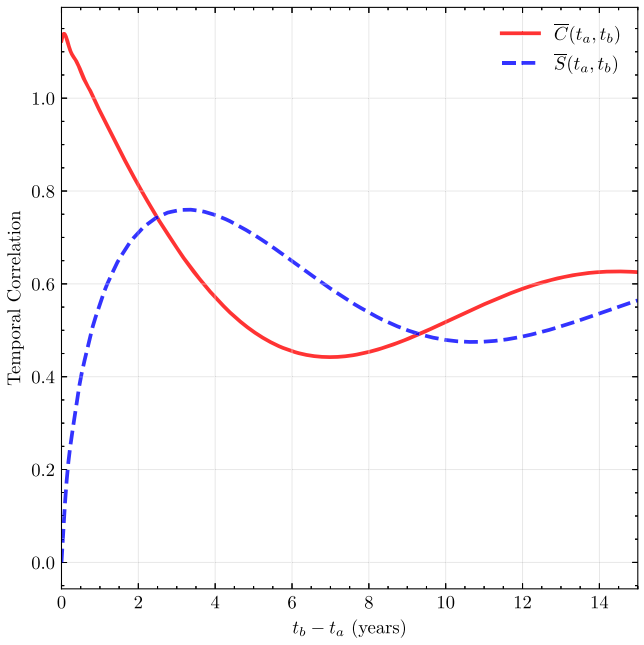
$$\langle r(t,\hat{e}_a)r(t,\hat{e}_b)\rangle = 2\int_0^\infty df\frac{\sin^2(\pi f t)}{(\pi f)^2}\sum_{\ell m}[I_{\ell m}(f)\mathrm{Re}[\gamma^I_{\ell m}(fD_a,fD_b,\zeta)] + iV_{\ell m}(f)\,\mathrm{Im}\,[\gamma^V_{\ell m}(fD_a,fD_b,\zeta)]]. \quad (52)$$

The pulsar timing residual correlation (53) shows that $\bar{C}(t,t')$ and $\bar{S}(t,t')$ are the temporal correlations associated with the intensity and circular polarization of the SGWB signal, respectively. Figure 4 shows that the temporal correlation $\bar{C}(t,t')$ is nonzero for all times t and t', while $\bar{S}(t,t')$ is nonzero only when $t\neq t'$. This means that the contribution by circular polarization vanishes at equal times, i.e., $\bar{S}(t,t)=0$. Figure 4 also shows spatial correlations that would be relevant to a circularly polarized SGWB signal; that is produced by a kinematic dipole (next section). These ORFs admit analytical expressions that were derived in the computational frame and can be found in [128]. We utilize these ORFs in the simulations of a circularly polarized SGWB signal in Sec. VI.

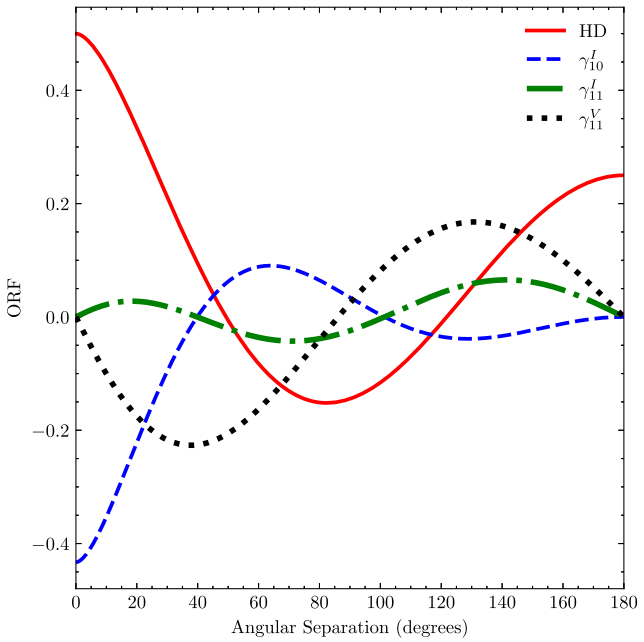
D. Kinematic dipole

It is instructive to see the circularly polarized signal produced by a kinematic boost, akin to the cosmic dipole.

We remind that anisotropy and circular polarization are distinct aspects of a signal, and that in practice it is possible to phenomenologically constrain these components by decomposing the signal in a given basis to tease out known signatures [124,125,127–131,140,146]). On the other hand, the kinematic dipole is of particular interest to cosmology due to debates about the cosmic dipole [147–154]. As we shall see, the kinematic boost supports both anisotropic and circularly polarized components which can be thought of as leading order corrections following the isotropic part of the signal. We stress out that GW and SGWB signals are naturally polarized to begin with, but that anisotropy is a separate ingredient needed to be experimentally sensitive to polarization. The advantage of this is that the cosmic



(a)



(b)

FIG. 4. (a) Temporal correlation in the timing residual correlation induced by a circularly polarized SGWB with a flat power spectrum, $I_{lm}(f)\sim$ Constant, $V_{lm}(f)\sim$ Constant, $T = 15$ years; $\bar{C}(t_a,t_b)$ (red solid) and $\bar{S}(t_a,t_b)$ (blue dashed) are temporal correlations associated with intensity and circular polarization, respectively, of the SGWB signal; (b) ORFs, $\gamma^I_{00}(\zeta) = \gamma^{\rm HD}(\zeta)$, $\gamma^I_{10}(\zeta)$, $\gamma^I_{11}(\zeta)$, and $\gamma^V_{11}(\zeta)$, in the computational frame for a circularly polarized SGWB [100,128,130].

dipole's direction and speed are known to a reasonable degree based on cosmological surveys. Thus, in theory, constraining the cosmic dipole in PTAs boils down to searching for well defined correlations modulo the HD curve in the timing residuals [124,125].

Consider a kinematic boost $\vec{v} = v\hat{v}$; magnitude v and direction $\hat{v}$. When applied, an initially isotropic circularly polarized SGWB will acquire a dipole anisotropy to leading order in v/c

$$I(f,\hat{k}) = I_{00}(f)[1+\beta(1-n_I(f))\hat{k}\cdot\hat{v}],$$
$$V(f,\hat{k}) = V_{00}(f)[1+\beta(1-n_V(f))\hat{k}\cdot\hat{v}], \tag{56}$$

where $\beta = v/c \ll 1$, and

$$n_I(f) = \frac{d\,\ln I_{00}(f)}{d\,\ln f}, \qquad n_V(f) = \frac{d\,\ln V_{00}(f)}{d\,\ln f}. \tag{57}$$

Expanding $\hat{k}\cdot\hat{v}$ in spherical harmonics (Appendix B),

$$\hat{k}\cdot\hat{v} = \frac{4\pi}{3}\sum_{m=-1}^{1} Y^*_{1m}(\hat{v})Y_{1m}(\hat{k}), \tag{58}$$

the dipole components of the Stokes parameters become

$$I_{1m}(f) = \frac{4\pi}{3}I_{00}(f)\beta[1-n_I(f)]Y^*_{1m}(\hat{v}),$$
$$V_{1m}(f) = \frac{4\pi}{3}V_{00}(f)\beta[1-n_V(f)]Y^*_{1m}(\hat{v}). \tag{59}$$

Now, consider a circularly polarized SGWB characterized by these dipole components. Recall that $\gamma^V_{00} = \gamma^V_{10} = 0$, $\gamma^V_{1-1} = \gamma^V_{11}$, and $\gamma^I_{1-1} = -\gamma^I_{11}$. Therefore, we have

$$\sum_{\ell m} I_{\ell m}(f)\gamma^I_{\ell m}(f,\zeta)$$
$$= I_{00}(f)[\gamma^I_{00}(f,\zeta) + \beta(1-n_I(f))$$
$$\times\left(\gamma^I_{10}(f,\zeta)\sqrt{\frac{4\pi}{3}}\cos\theta_v\right.$$
$$\left.-\gamma^I_{11}(f,\zeta)\sqrt{\frac{8\pi}{3}}\sin\theta_v\cos\phi_v\right)], \tag{60}$$

and

$$i\sum_{\ell m} V_{\ell m}(f)\gamma^V_{\ell m}(f,\zeta) = V_{00}(f)\gamma^V_{11}(f,\zeta)\beta(1-n_V(f))$$
$$\times\sqrt{\frac{8\pi}{3}}\sin\theta_v\sin\phi_v. \tag{61}$$

We emphasize that in the above expression, the dipole direction (θ_v, ϕ_v) is given in the computational frame [100,127–131]. This is an important consideration when simulating the circularly polarized signal due to a kinematic dipole and plays a crucial role in constructing the covariance matrix $\mathbf{\Sigma}$ (see Secs. IV and VI or Appendix C).

E. Transfer functions

Building on Sec. III C, we now extend the transfer function formalism to the case of a circularly polarized SGWB, using the timing residual correlation (53). The goal is to express the correlations between Fourier components across frequency bins, as in Sec. II, and to identify the transfer functions that govern the imprint of circular polarization on the PTA data.

The relevant Fourier correlations are given by

$$\begin{aligned}\langle \alpha_{aj}\alpha_{bk}\rangle &= \left(\frac{2}{T}\right)^2 \iint_0^T dt\, dt' \langle r(t,\hat{e}_a) r(t',\hat{e}_b)\rangle \sin(\omega_j t)\sin(\omega_k t') \\ &= \int_0^\infty \frac{2df}{(2\pi f)^2} \mathcal{C}^{\alpha}_{j,k}(f) \sum_{\ell m} I_{\ell m}(f)\gamma^I_{\ell m}(fD_a, fD_b, \hat{e}_a\cdot\hat{e}_b), \end{aligned} \tag{62}$$

$$\begin{aligned}\langle \beta_{aj}\beta_{bk}\rangle &= \left(\frac{2}{T}\right)^2 \iint_0^T dt\, dt' \langle r(t,\hat{e}_a) r(t',\hat{e}_b)\rangle \cos(\omega_j t)\cos(\omega_k t') \\ &= \int_0^\infty \frac{2df}{(2\pi f)^2} \mathcal{C}^{\beta}_{j,k}(f) \sum_{\ell m} I_{\ell m}(f)\gamma^I_{\ell m}(fD_a, fD_b, \hat{e}_a\cdot\hat{e}_b), \end{aligned} \tag{63}$$

$$\begin{aligned}\langle \alpha_{aj}\beta_{bk}\rangle &= \left(\frac{2}{T}\right)^2 \iint_0^T dt\, dt' \langle r(t,\hat{e}_a) r(t',\hat{e}_b)\rangle \sin(\omega_j t)\cos(\omega_k t') \\ &= \int_0^\infty \frac{2df}{(2\pi f)^2} \mathcal{C}^{\alpha\beta}_{j,k}(f) \sum_{\ell m} iV_{\ell m}(f)\gamma^V_{\ell m}(fD_a, fD_b, \hat{e}_a\cdot\hat{e}_b), \end{aligned} \tag{64}$$

$$\begin{aligned}\langle \beta_{aj}\alpha_{bk}\rangle &= \left(\frac{2}{T}\right)^2 \iint_0^T dt\, dt' \langle r(t,\hat{e}_a) r(t',\hat{e}_b)\rangle \cos(\omega_j t)\sin(\omega_k t') \\ &= \int_0^\infty \frac{2df}{(2\pi f)^2} \mathcal{C}^{\beta\alpha}_{j,k}(f) \sum_{\ell m} iV_{\ell m}(f)\gamma^V_{\ell m}(fD_a, fD_b, \hat{e}_a\cdot\hat{e}_b), \end{aligned} \tag{65}$$

where $\mathcal{C}^{\alpha}_{j,k}(f)$ and $\mathcal{C}^{\beta}_{j,k}(f)$ are the transfer functions previously defined in (22)-(23), while the new transfer functions corresponding to the circular polarization components, $\mathcal{C}^{\alpha\beta}_{j,k}(f)$ and $\mathcal{C}^{\beta\alpha}_{j,k}(f)$, are given by

$$\begin{aligned}\mathcal{C}^{\alpha\beta}_{j,k}(f) &= \left(\frac{2}{T}\right)^2 \iint_0^T dt\, dt' \,\mathrm{Im}[C(f,t_a,t_b)]\sin(\omega_j t)\cos(\omega_k t'), \\ \mathcal{C}^{\beta\alpha}_{j,k}(f) &= \left(\frac{2}{T}\right)^2 \iint_0^T dt\, dt' \,\mathrm{Im}[C(f,t_a,t_b)]\cos(\omega_j t)\sin(\omega_k t'), \end{aligned} \tag{66}$$

with $\mathrm{Im}[C(f,t_a,t_b)]$ defined in (54). Importantly, only the terms involving the relative time difference contribute to these integrals, reflecting the physical origin of the circular polarization signal.

Carrying out the time integrations, we arrive at explicit expressions for the circular polarization transfer functions[12]:

[12]As with the α- and β- transfer functions, the circular polarization transfer functions can be written as

$$\begin{aligned}\mathcal{C}^{\alpha\beta}_{j,k}(f) &= -\frac{4(-1)^{j+k} f_j f}{(f+f_j)(f+f_k)} \mathrm{sinc}(\pi T(f-f_j))\mathrm{sinc}(\pi T(f-f_k)), \\ \mathcal{C}^{\beta\alpha}_{j,k}(f) &= \frac{4(-1)^{j+k} f f_k}{(f+f_j)(f+f_k)} \mathrm{sinc}(\pi T(f-f_j))\mathrm{sinc}(\pi T(f-f_k)). \end{aligned}$$

These are directly related to the imaginary components of the correlation in the exponential Fourier basis (Appendix A).

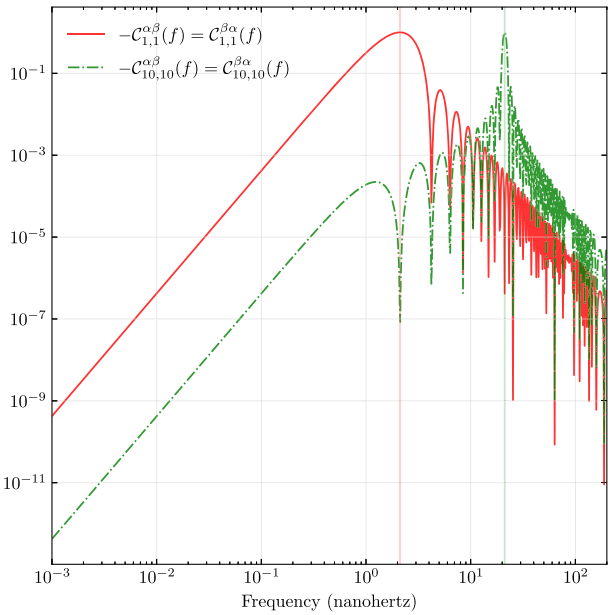
$$\mathcal{C}^{\alpha\beta}_{j,k}(f) = -\frac{4f_j f}{\pi^2 T^2}\frac{\sin^2(\pi f T)}{(f^2-f_j^2)(f^2-f_k^2)},$$
$$\mathcal{C}^{\beta\alpha}_{j,k}(f) = \frac{4f_k f}{\pi^2 T^2}\frac{\sin^2(\pi f T)}{(f^2-f_j^2)(f^2-f_k^2)}. \quad (67)$$

An unpolarized SGWB can now be viewed as the limit when the cross terms $\langle\alpha_{aj}\beta_{bk}\rangle$ and $\langle\beta_{aj}\alpha_{bk}\rangle$ vanish. Thus, the transfer functions (22)–(23) are associated with the intensity (unpolarized) component of the signal. The new transfer functions (67) capture the imprint of circular polarization.

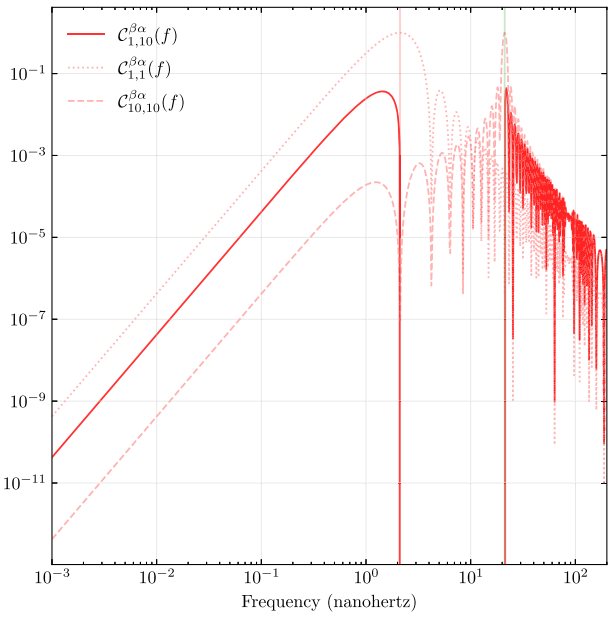
This formalism reveals how circular polarization introduces distinctive correlations between the sine and cosine Fourier coefficients of the timing residuals, encoded in the nonzero $\langle\alpha_{aj}\beta_{bk}\rangle$ and $\langle\beta_{aj}\alpha_{bk}\rangle$ terms. The structure and frequency dependence of these transfer functions provide a clear pathway for identifying and characterizing anisotropic circular polarization signatures in PTA data, complementing the standard intensity analysis and opening new avenues for probing the polarization content of the SGWB [124,125,127–131,140,146,155].

Figure 5 illustrates the transfer functions associated with the circular polarization component of the SGWB, as given in Eq. (67). These transfer functions play an analogous role to those for the intensity component, encoding how a broadband circular polarization signal is distributed across the finite time Fourier bins of the PTA residuals. As with the intensity case, the diagonal elements ($j = k$) exhibit a pronounced mainlobe centered at $f = f_k$, accompanied by sidelobes reminiscent of a far-field radiation pattern. This structure highlights that the dominant contribution to the cross-correlation between sine and cosine Fourier components, $\langle\alpha_{ak}\beta_{bk}\rangle = -\langle\beta_{ak}\alpha_{bk}\rangle$, comes from the adjacent neighborhood (mainlobe) of the frequency f_k. The off-diagonal (cross-frequency, $j \neq k$) transfer functions are suppressed, indicating that correlations between different frequency bins due to circular polarization are subdominant, mirroring the behavior found for the intensity transfer functions. This reinforces the general picture developed in the previous sections: the main features of the SGWB signal, whether unpolarized or circularly polarized, are captured by the diagonal transfer functions, while cross-frequency correlations remain small (but non-negligible, as shown in Ref. [118]).

Another observation that we wish to spotlight is the negative sign in the relation $C^{\alpha\beta}_{k,k}(f) = -C^{\beta\alpha}_{k,k}(f)$ between the circular polarization transfer functions. This invokes that $\langle\alpha_{ak}\beta_{bk}\rangle = -\langle\beta_{ak}\alpha_{bk}\rangle$, and so (for $a = b$) imposes that $\langle\alpha_{ak}\beta_{ak}\rangle = \langle\beta_{ak}\alpha_{ak}\rangle = 0$. The autocorrelation terms vanish; or rather, the cross-Fourier components, $\langle\alpha_{aj}\beta_{bk}\rangle$, are only correlated across different pulsars ($a \neq b$). The implies that the signature of circular polarization is distinctly in the cross-correlated power across pulsars or pulsar pairs.



(a) circular polarization transfer functions (67) for $j = k$



(b) cross frequency transfer functions $j \neq k$

FIG. 5. Representative transfer functions for circular polarization (67) in a PTA residuals' Fourier components with $T = 15$ years, $f_1 \sim 2.1$ nanohertz, and $f_k \sim k f_1$.

VI. COMPARISON WITH SIMULATION

As we did to understand the properties of the unpolarized SGWB signal, we motivate our results for a circularly polarized SGWB by comparing with simulations.

For the simulation, we proceed by extending the framework given in Sec. IV (or Appendix C) to include circular polarization components. Specifically, we generalize the covariance matrix $\mathbf{\Sigma}$ to

$$\Sigma^k_{ab} = \begin{pmatrix} \langle \alpha_{ak}\alpha_{bk}\rangle & \langle \alpha_{ak}\beta_{bk}\rangle \\ \langle \beta_{ak}\alpha_{bk}\rangle & \langle \beta_{ak}\beta_{bk}\rangle \end{pmatrix}. \tag{68}$$

The Gaussian unpolarized SGWB signal can be recovered by setting $\langle \alpha_{ak}\beta_{bk}\rangle = \langle \beta_{ak}\alpha_{bk}\rangle = 0$; decoupling the sine- and cosine-Fourier coefficients of pulsar pairs. In addition, we consider a standard power-law (33) for the intensity and circular polarization power spectra ($n_I = n_V = 2 - \gamma_{\rm gw}$). We define the constant $\Pi = |V_{00}(f)/I_{00}(f)| \leq 1$ as an indicator of the degree of circular polarization of the signal. $\Pi = 1$ corresponds to a hundred percent circularly polarized signal. Then, assuming a constant Π, we write down the components of the covariance matrix as

$$\langle \alpha_{ak}\alpha_{bk}\rangle = \Gamma^I(\hat{e}_a\cdot\hat{e}_b)\int_{f_{\rm min}}^{f_{\rm max}} df S(f)\mathcal{C}^{\alpha}_{k,k}(f), \tag{69}$$

$$\langle \beta_{ak}\beta_{bk}\rangle = \Gamma^I(\hat{e}_a\cdot\hat{e}_b)\int_{f_{\rm min}}^{f_{\rm max}} df S(f)\mathcal{C}^{\beta}_{k,k}(f), \tag{70}$$

$$\langle \alpha_{ak}\beta_{bk}\rangle = \Gamma^V(\hat{e}_a\cdot\hat{e}_b)\Pi\int_{f_{\rm min}}^{f_{\rm max}} df S(f)\mathcal{C}^{\alpha\beta}_{k,k}(f), \tag{71}$$

$$\langle \beta_{ak}\alpha_{bk}\rangle = \Gamma^V(\hat{e}_a\cdot\hat{e}_b)\Pi\int_{f_{\rm min}}^{f_{\rm max}} df S(f)\mathcal{C}^{\beta\alpha}_{k,k}(f), \tag{72}$$

where the spatial correlation functions are

$$\begin{aligned}\Gamma^I(\hat{e}_a\cdot\hat{e}_b) = (1+\delta_{ab})\Bigg[&\mathbf{\Gamma}(\hat{e}_a\cdot\hat{e}_b) + \beta(1-n_I)\\ &\times\left(\mathbf{\Gamma}^I_{10}(\hat{e}_a\cdot\hat{e}_b)\sqrt{\frac{4\pi}{3}}\cos\theta_v\right.\\ &\left.-\mathbf{\Gamma}^I_{11}(\hat{e}_a\cdot\hat{e}_b)\sqrt{\frac{8\pi}{3}}\sin\theta_v\cos\phi_v\right)\Bigg],\end{aligned} \tag{73}$$

$$\Gamma^V(\hat{e}_a\cdot\hat{e}_b) = \mathbf{\Gamma}^V_{11}(\hat{e}_a\cdot\hat{e}_b)\beta(1-n_V)\sqrt{\frac{8\pi}{3}}\sin\theta_v\sin\phi_v. \tag{74}$$

The ORFs $\mathbf{\Gamma}_{lm}(\hat{e}_a\cdot\hat{e}_b)$'s are shown in the right panel of Fig. 4; where the leading term is the HD curve (17). The bold faced ORFs $\mathbf{\Gamma}^X_{lm}$ (as shown in Fig. 3) are normalized as $\mathbf{\Gamma} = 1/2$ in the limit $\hat{e}_a\cdot\hat{e}_b = 1^-$ and $D_a = D_b$. Their analytical expressions can be found in Ref. [128]. Note that the correction terms are controlled by two quantities; the dipole speed ratio $\beta = v/c \sim \mathcal{O}(10^{-3})$ and the degree of circular polarization $\Pi \leq 1$. Above all, in this formulation, we emphasize that the terms of the covariance must be built in the computational frame where the ORFs take on the particular shapes drawn in Refs. [100,128,156,157] (see Fig. 4).

Fixing $A_{\rm gw} = 10^{-15}$, $\gamma_{\rm gw} = 13/3$ (SMBHB), $\beta = v/c = 10^{-3}, 10^{-1}$, and a 100% circular polarization ($\Pi = 1$), we obtain Fig. 6 using simulated pulsar timing residuals with 100 pulsars at fixed sky positions. The dipole is arbitrarily pointed to the y direction. The same results are shown in Appendix F or Fig. 8, but with standard errors to show the variations expected across realizations in the computational frame; as one representative of frame dependent methods.

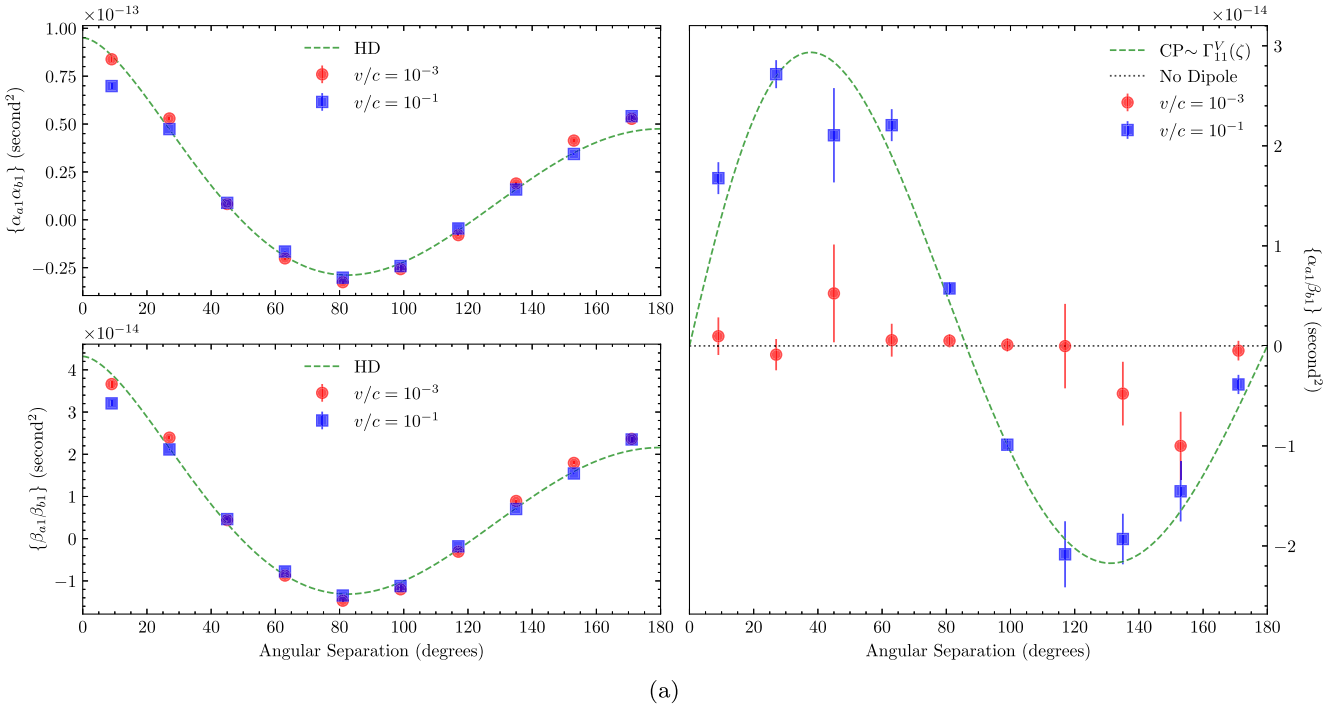
The procedure for computing the sample averages is similar to the isotropic case described in Sec. IV: we compute the Fourier coefficients and then evaluate the sample statistics as in Eq. (34). However, a key difference for the circular polarization case is the need to work in the computational frame to recover the anisotropic signal. Specifically, for each realization of the PTA data, we arbitrarily select one pulsar as a and treat the remaining pulsars as b's, thereby forming $n_{\rm psrs} - 1$ pairs per realization. This is in contrast to the isotropic case, where all unique pulsar pairs are used, yielding $n_{\rm psrs}(n_{\rm psrs} - 1)/2$ pairs and thus greater statistical power.

The requirement to analyze in the computational frame is limited to the context of this work since the ORFs considered (shown in Fig. 4) have been derived in the computational frame [127,128]. In practice, a frequentist targeted search can be performed to look for nonisotropic signals, by constructing a matched filter response or a detection statistic that is the dot product between the data and an anisotropic distribution of GW power with known polarization content in a fixed reference frame [158,159]. Other (possibly related) alternatives are to work in celestial coordinates and a bipolar spherical harmonics basis [100,146]. Either way, the computational frame is also representative of frame dependent methods, and frame dependent methods do not perform pulsar averaging because this will wash out the sensitivity to anisotropic signals.

For each (a, b) pair, we rotate pulsar a to the z-axis and pulsar b into the xz-plane ($\phi = 0$), following the standard computational frame convention. The corresponding rotation matrices are then used to determine the dipole direction (θ_v, ϕ_v) in this frame, which is required to evaluate the cross-Fourier spatial correlation [see Eq. (74)]. To account for the dipole orientation, we compute the normalized statistic $\alpha_{ak}\beta_{bk}/(\sin\theta_v\sin\phi_v)$ for all $n_{\rm psrs} - 1$ pairs in each realization.

An important consequence of this approach is that, because we do not average over all unique pulsar pairs, the ensemble variance of the recovered statistic converges to the larger pulsar variance rather than the cosmic variance [101,160–162]. Nevertheless, this method enables us to recover the circularly polarized SGWB signal when the dipole speed is artificially increased, as demonstrated in Fig. 6.

Our simulations demonstrate that the circularly polarized SGWB signal supported by a kinematic dipole can be recovered when the dipole speed is artificially increased by one to two orders of magnitude above its physical value



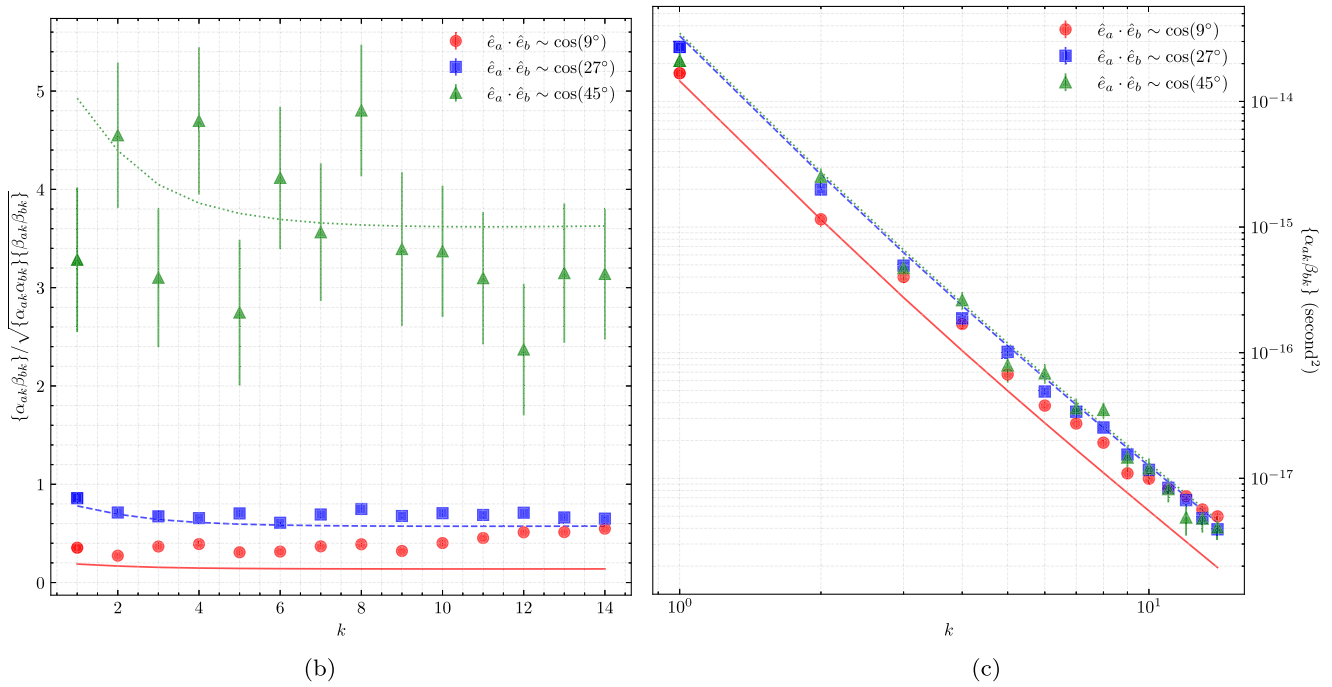


FIG. 6. Top panel: two-point correlation functions and bottom panel: the bin power of the Fourier coefficients of pulsar timing residuals for a simulated 15-year PTA dataset with a circularly polarized SGWB signal. Each one of 10^4 realizations has 100 pulsars at fixed positions. The error bars shown are the error on the mean. The SGWB characteristic strain and spectral index are $A_{\rm gw} = 10^{-15}$ and $\gamma_{\rm gw} = 13/3$, respectively. The kinematic dipole (along the y direction) has a speed $\beta = v/c = 10^{-3}, 10^{-1}$, and the degree of circular polarization is $\Pi = 1$. In the top panel, the green dashed lines represent the Gaussian theoretical expectation values. In the bottom panel, the colored curves (red-solid, blue-dashed, and green-dotted) represent the Gaussian theoretical expectation values of the frequency-bin power of the cross-Fourier statistic $\{\alpha_{ak}\beta_{bk}\}$ at $9°, 27°, 45°$ angular bins, or $\hat{e}_a \cdot \hat{e}_b \sim \cos(9°), \cos(27°), \cos(45°)$.

($v/c \sim 10^{-3}$). For realistic dipole speeds, however, the circular polarization signal is suppressed by a factor of v/c relative to the leading isotropic component, rendering its detection extremely challenging in practice. As expected, the HD correlation is robustly recovered in the $\langle \alpha_{ak}\alpha_{bk}\rangle$ and $\langle \beta_{ak}\beta_{bk}\rangle$ Fourier bins (see Fig. 6, top left panel).

In principle, there are also v-dependent corrections to the HD correlation [see Eqs. (60) and (73)] that could, in theory, be used to probe the kinematic dipole. However, these corrections are suppressed by a factor of $v/c \sim 10^{-3}$ relative to the HD curve and are not expected to be detectable due to the dominant cosmic variance [101,160–162].

When discussing the signal of circular polarization, the focus is on the cross-Fourier components $\langle \alpha_{ak}\beta_{bk}\rangle$ and $\langle \beta_{ak}\alpha_{bk}\rangle$, which become nonzero in the presence of a circularly polarized SGWB. The top right panel of Fig. 6 shows that these cross-Fourier components are indeed nonzero and match the Gaussian theoretical expectation, being proportional to $\mathbf{\Gamma}^{V}_{11}(\hat{e}_a \cdot \hat{e}_b)$ (see Fig. 4). The bottom panels of Fig. 6 display the frequency-bin power of the cross-Fourier statistic $\{\alpha_{ak}\beta_{bk}\}$ at selected angular bins, corresponding to $\hat{e}_a \cdot \hat{e}_b \sim \cos(9°), \cos(27°), \cos(45°)$. The bin power due to circular polarization, $\langle \alpha_{ak}\beta_{bk}\rangle$ or $\langle \beta_{ak}\alpha_{bk}\rangle$, falls off with frequency faster than $\langle \alpha_{ak}\alpha_{bk}\rangle$ but slower than $\langle \beta_{ak}\beta_{bk}\rangle$. This behavior reflects the frequency dependence of the circular polarization transfer functions (67), which lie between the α- and β-transfer functions in their fall off.

Recall that, for a Gaussian unpolarized SGWB, the Fourier coefficients α_{ak} and β_{bk} are uncorrelated in a pulsar and in pulsar pairs. In contrast, the presence of a circularly polarized SGWB—such as that supported by a kinematic dipole—generates a distinctive, nonzero cross-correlation between the sine and cosine Fourier components of the timing residuals across pulsar pairs. To our knowledge, this cross-Fourier correlation is a unique signature of circular polarization in the SGWB and is not expected to arise from other known astrophysical sources in PTA data.

Our simulations of a Gaussian circularly polarized SGWB signal yield several important insights. First, the reliance on the computational frame restricts us from performing a full-sky average, which significantly limits the statistical power of the analysis. For realistic dipole amplitudes, the circular polarization signal is so weak that it is easily buried in the statistical fluctuations (pulsar variance [101,162]) of any single realization. Even when the dipole speed is artificially amplified, summing over all pulsar pairs in a PTA can obscure the anisotropic signal due to the frame dependence. This highlights a key limitation: the computational frame, while convenient for theoretical calculations, is not optimal for extracting circular polarization signatures in practice. Developing methods to simulate and recover circular polarization without relying on the computational frame such as performing harmonic expansions in the celestial frame [see Eq. (45)] or using bipolar spherical harmonics [100] would be a valuable direction for future work.

While our analysis is statistically limited by the use of the computational frame, our results suggest that the circularly polarized signal associated with the kinematic dipole deserves further investigation. In particular, a robust detection or constraint of this signal could provide an independent probe of the cosmic dipole as PTA sensitivity improves in the coming decade.

Lastly, we return to the anisotropic signal corrections due to a kinematic dipole; that appear as extra terms in (73) following the HD curve. Similar questions have been addressed in [124,125] where the anisotropic and circularly polarized components were studied separately. At leading order in the dipole's speed with respect to the speed of light, a kinematic dipole sources anisotropic and polarized components in the pulsar timing residual correlation through the SGWB. While our attention was focused on circular polarization due to its unique signature of coupling odd and even Fourier modes through the sample averages of $\alpha_{ak}\beta_{bk}$, we have included as well anisotropic corrections in the simulations. This explains why the sample averages of $\alpha_{ak}\alpha_{bk}$ and $\beta_{ak}\beta_{bk}$ show small deviations relative to the HD curve in Fig. 6. However, these leading-order anisotropic terms are suppressed by a factor v/c compared to the HD curve. This is the reason the deviation to the HD curve due to anisotropy remained small even when the dipole's speed was artificially increased to a tenth of the speed of light. That is, the corrections were at most ten percent compared to the dominant isotropic component. Nonetheless, it is possible to dissect the anisotropic corrections due to a kinematic dipole as illustrated in [124] by utilizing specific geometric orientations relative to the dipole's direction. Our results in this direction of a purely anisotropic signal are teased out in Appendix G. The level of anisotropic correction $\mathcal{O}(v/c)$ and the attention that anisotropic searches receive have motivated us to focus on the circularly polarized correction.

VII. DISCUSSION

We wrap up with a Q&A-like section that goes through very briefly (what we subjectively think are) the most conceptually interesting aspects of the work.

A. Why are the variances of the sine- and cosine-Fourier coefficients different?

The short answer is that the Fourier basis $\{\sin(2\pi kt/T_{\rm obs}), \cos(2\pi kt/T_{\rm obs})\}$ does not diagonalize the covariance of a signal with a characteristic timescale $T_{\rm s} \gg T_{\rm obs}$. Physically, this is because the observation modes are unavoidably misaligned with the signal's harmonics due to the enormous timescale difference.

Consider a stationary process $y(t)$ with zero mean, $\langle y(t)\rangle = 0$, and covariance $\langle y(t)y(t')\rangle = \mathcal{C}(|t-t'|)$. The Wiener-Khinchin theorem relates this to a power spectral density $\mathcal{S}(f)$ via

$$\mathcal{C}(\tau) = \int_0^\infty df \mathcal{S}(f)\cos(2\pi f\tau). \tag{75}$$

For a signal with characteristic timescale T_s and a set of fundamental frequencies $\{f_j = j/T_s, j\in\mathbb{N}\}$, the time-domain covariance matrix $K_{ij} = C(|t_i - t_j|)$ can be expressed as a Riemann sum over these modes[13]:

$$K_{ij} = \sum_{k=1}^{\infty} \Delta f_k \mathcal{S}(f_k)[\cos(\omega_k t_i)\cos(\omega_k t_j) + \sin(\omega_k t_i)\sin(\omega_k t_j)], \tag{76}$$

where $\Delta f_k = 1/T_s$ and $\omega_k = 2\pi f_k = 2\pi k/T_s$. Clearly, the signal covariance is naturally diagonalized in a Fourier basis $\{\sin(2\pi kt/T_s), \cos(2\pi kt/T_s)\}$, with the sine and cosine coefficients both having variances proportional to $\mathcal{S}(f_k)$.

However, in practice, observations are limited to a finite time window $T_{obs} \ll T_s$, and the observational frequency basis $\{f_k = k/T_{obs}\}$ no longer aligns with the signal's intrinsic modes. Consequently, the covariance matrix will not be diagonal in the observational basis $\{\sin(2\pi kt/T_{obs}), \cos(2\pi kt/T_{obs})\}$, and the sine and cosine Fourier coefficients will generally have unequal variances. This is especially relevant for PTA searches, where the gravitational-wave (GW) timescale is $\mathcal{O}(10^9)$ years, vastly longer than the typical observational baseline of $\mathcal{O}(10)$ years [108].

We emphasize that the signal is not periodic. Above, the timescale T_s parametrizes the harmonic space frequencies of a signal, such that each adjacent harmonics are separated by T_s^{-1}, i.e., $\Delta f_k = f_k - f_{k-1} = T_s^{-1}$. In general, a signal's harmonic frequencies do not have to lie on an equally spaced lattice, the arguments can be generalized, and our simplified usage only highlights physical concepts at play.

A key implication is that approximating the covariance as diagonal in the observational Fourier basis [16] neglects the frequency correlations, leading to systematic biases in parameter estimation [117,118]. The GW signal characteristic timescale can be estimated using Peters' timescale [163,164]; for an equal mass binary (each with mass m and a separation r) this gives $T_{gw} \sim 5c^5 r^4/(256G^3m^3) \sim 5.8\times 10^8\ \mathrm{yr}(r/1\ \mathrm{pc})^4(10^{10}M_\odot/m)^3$.

[13]Equivalently, one may expand $\mathcal{S}(f)$ as a sum over delta functions at the signal's harmonic frequencies: $\mathcal{S}(f) = \sum_k s_k\delta(f-f_k)$.

B. Are the so-called transfer functions discussed throughout special for PTA?

No. The transfer functions defined in Eqs. (22)–(23) are not exclusive to PTAs but arise generically when a stationary, temporally correlated process is observed over a finite time window. This situation arises in time series analyses involving correlated processes such as intrinsic red noise in pulsars.

These transfer functions encapsulate how the signal is projected onto a Fourier basis with a finite time window. As the duration of observation increases and approaches the signal's intrinsic timescale, the transfer functions asymptotically approach delta functions centered at the signal's natural frequencies, thereby recovering the ideal decomposition.

This can also be realized by writing Eqs. (22)–(23) in terms of the finite time approximation to the delta function, $\delta_T(x) = T\mathrm{sinc}(\pi xT)$. As $T\to\infty$, the α-transfer function approaches the β-transfer function. Then, $\langle\alpha_{aj}\alpha_{bk}\rangle/\langle\beta_{aj}\beta_{bk}\rangle \to 1$ and hence the Fourier mode decomposition of the covariance function $\langle r(t)r(t')\rangle$ in Eq. (30) reduces to a sum of $\cos(w_k(t-t'))$.

C. What are the prospects for detecting circular polarization in the SGWB?

Our results indicate that detecting circular polarization in the SGWB will be challenging. Let us begin with the encouraging aspects: circular polarization induces a unique cross-correlation between the sine and cosine Fourier coefficients of different pulsars (see Fig. 6). This coupling produces a distinctive spatial correlation pattern and associated power spectrum that, in principle, could be extracted from data. Furthermore, such a signal might contain information about the anisotropic distribution of sources [130].

On the downside, the signal supported by a kinematic dipole with velocity $v/c \sim 10^{-3}$ is expected to lie well below the cosmic variance threshold set by the HD correlation [101,160,161], and subsequently also below instrumental noise.

Despite these challenges, the circularly polarized component of the SGWB can still be constrained phenomenologically by measuring the cross-correlated power between the sine and cosine Fourier coefficients across pulsar pairs. This motivates a likelihood analysis that does not depend on the computational frame, enabling full sky averaging with PTA data to resolve circular polarization. Developing such methods remains an open area for future research. We also refer the reader to the important works [124,125,127–131,140,146] for leading the way to this direction.

Anisotropy, polarization and the kinematic dipole are independent concepts, and in this work we used the kinematic dipole (motivated cosmologically through CMB and large scale structure observations) to tease out

leading order corrections following an isotropic PTA signal. We refer the reader to the works cited in the preceding paragraphs for applications beside a kinematic dipole.

D. Can a PTA be used to probe the cosmic dipole?

In theory, yes. If the SGWB originates from cosmological sources, a leading order dipolar anisotropy arising from our motion relative to the cosmic rest frame should imprint a characteristic correction of the order of $v/c \sim 10^{-3}$. This kinematic dipole is of considerable cosmological interest [147–154,165–167], especially in light of ongoing efforts to test the consistency of the cosmological principle using independent large scale observables such as the CMB and quasar catalogs (see e.g., [153] and Sec. 2.3.6 of [166]).

PTAs offer a novel opportunity to detect this dipolar signature via its characteristic spectral and spatial correlations in the timing residuals. However, this is contingent upon the SGWB being predominantly cosmological. If instead the SGWB is dominated by astrophysical sources, then the intrinsic anisotropies are likely to be much larger, potentially obscuring the kinematic dipole [124,125,155].

Detecting the cosmic dipole thus remains an ambitious goal for PTA science.

VIII. CONCLUSIONS

In this work, we have revisited the formulation of the stochastic gravitational wave background (SGWB) signal in pulsar timing arrays (PTAs), providing a unified frequency- and Fourier-domain framework that connects theoretical predictions with simulation results. By comparing Gaussian theoretical expectation values with both standard point-source simulations and our own covariance-matrix-based approach, we have demonstrated the robustness of this framework for both isotropic unpolarized (Secs. III–IV) and circularly polarized (Secs. V–VI) SGWB signals.

A central result of our analysis is the identification and explicit construction of transfer functions in the Fourier basis that factor in frequency correlations that occur due to the observing a temporally correlated signal in a finite time window. We have shown that the correlations of the Fourier coefficients of pulsar timing residuals can be accurately described by convolving these transfer functions with the relevant power spectra or power spectral densities. This approach, detailed in Eqs. (28)–(29) and Eqs. (22)–(26), provides a simple yet powerful prescription for modeling the SGWB signal in the frequency- and Fourier-domain, complementary to time-domain methods that have been mainly utilized in PTA analysis. Our results further indicate that static and cross-frequency effects, while present, are subdominant. Cross-frequency effects were nonetheless given the spotlight in Ref. [118], showing their importance in mitigating biased parameter estimates.

We emphasize that the diagonals considered in this work fully account for interfrequency correlations through the accommodation of transfer functions; and are distinct to the diagonals of the diagonal covariance approximation often adopted for PTA analysis. The diagonal covariance approximation was a milestone in PTA analysis for a practical reason: computing the off diagonal terms take significantly more time compared to the diagonals. It is the same practicality that has driven us to focus on the diagonals, and we could take the agreement between the point source-based TEMPO2 simulations and our results as a validation. However, this is not a guarantee that the off-diagonals can be left out of practical applications and it is important to pay attention to their contribution to avoid systematic biases. This is a work that we have in mind in the future.

Importantly, the transfer functions do not rely on any new assumptions about the SGWB, but instead emerge directly from the temporal structure of any correlated signal; on equal footing with the Hellings-Downs curve and the power spectrum in characterizing the SGWB in PTA data.

Looking ahead, several promising directions emerge from this work. First, incorporating transfer functions into postfit analyses would help mitigate systematic biases in SGWB parameter estimation in the frequency- and Fourier-domain. Second, exploring simulation strategies for circularly polarized signals that do not rely on the computational frame and other frame dependent strategies would enable more robust statistical analyses and facilitate full sky averaging. Frame dependent frequentist targeted searches are often used in practice which utilizes estimators of the spherical harmonic components of the GW power with known spatial distribution and polarization. Third, the transfer function formalism motivates a renewed examination of subnanohertz GW contributions in PTA data, which may reveal new physical insights as PTA sensitivity improves [168,169]. Finally, extending this framework to include intrinsic pulsar red noise, white measurement noise, and higher-order statistics [106,122] will be important for future PTA analyses and for testing the Gaussianity of the SGWB signal.

Overall, our results highlight the importance of temporal correlations and transfer functions in the accurate modeling and interpretation of SGWB signals in PTAs, and provide a foundation for future developments in both theoretical and simulation-based PTA analyses.

ACKNOWLEDGMENTS

The authors thank Stephen Appleby for relevant discussion on correlated variables, Adrian Villanueva on GW timescales, Guillem Domènech for pointing out typos in a preliminary draft, and Xiao Xue for important comments on detecting circular polarization in a PTA. The authors are grateful to Bruce Allen, Rutger van Haasteren, and Boris

Goncharov for various important discussions that have influenced the development of this work. R. C. B. was supported by an appointment to the JRG Program at the APCTP through the Science and Technology Promotion Fund and Lottery Fund of the Korean Government, and was also supported by the Korean Local Governments in Gyeongsangbuk-do Province and Pohang City. This work was supported in part by the National Science and Technology Council of Taiwan, Republic of China, under Grant No. NSTC 113-2112-M-001-033. R. C. B. is grateful to the Institute of Physics, Academia Sinica for the hospitality that enabled the completion of this work. The authors are grateful to the participants of the external program APCTP-GW2025 [or APCTP2025-E05] held at Academia Sinica, Taipei, Taiwan for fruitful discussions.

DATA AVAILABILITY

The data that support the findings of this article are openly available [143].

APPENDIX A: A CHOICE OF BASIS FUNCTIONS

The pulsar timing residual, $r(t,\hat{e})$, or any time series, in a domain $t\in(t_i,t_i+T)$ for some initial time t_i can be interpreted as Eq. (1). This can be done because the sines and cosines over the domain $t\in(0,T)$ form a complete basis;

$$\int_0^T \frac{2dt}{T}\sin(\omega_j t)\sin(\omega_k t)=\delta_{jk}, \tag{A1}$$

$$\int_0^T \frac{2dt}{T}\cos(\omega_j t)\cos(\omega_k t)=\delta_{jk}, \tag{A2}$$

$$\int_0^T \frac{2dt}{T}\sin(\omega_j t)\cos(\omega_k t)=0, \tag{A3}$$

where $\omega_j=2\pi j/T$, and j, k are positive integers ($j,k\in\mathbb{N}$). This choice of basis functions is however arbitrary, and another common way a time data can be interpreted is by

$$r(t,\hat{e})=\sum_{k=-\infty}^{\infty}\psi_k(\hat{e})e^{i\omega_k t}, \tag{A4}$$

utilizing an exponential Fourier basis functions, e.g., in PTA science this has been used in Refs. [108,118]. In this case, the orthonormality of the basis functions can be expressed as

$$\int_{-T/2}^{T/2}\frac{dt}{T}e^{i(\omega_j-\omega_k)t}=\delta_{jk}. \tag{A5}$$

Then, the Fourier coefficients $\psi_k(\hat{e})$ can be obtained as

$$\psi_k(\hat{e})=\int_{-T/2}^{T/2}\frac{dt}{T}e^{-i\omega_k t}r(t,\hat{e}). \tag{A6}$$

Take note that the domain of the data has been shifted to $t\in(-T/2,T/2)$. This is always possible in practice. The two descriptions are equivalent, as will be shown.

In the exponential Fourier basis, the correlation between the Fourier coefficients of the pulsar timing residuals' (following analogous steps done in the main text, Sec. III) can be shown to be

$$\langle\psi_j(\hat{e}_a)\psi_k^*(\hat{e}_b)\rangle = \int_{f_{\min}}^{f_{\max}}\frac{2df}{(2\pi f)^2}\mathcal{C}_{j,k}(f)I(f)\gamma(fD_a,fD_b,\hat{e}_a,\hat{e}_b), \tag{A7}$$

where the corresponding transfer function is given by [108,118]

$$C_{j,k}(f)=\mathrm{sinc}(\pi T(f-f_j))\mathrm{sinc}(\pi T(f-f_k)). \tag{A8}$$

An important observation is that in this basis there is only one transfer function, $C_{j,k}(f)$, due to the phase symmetry of the exponential sum, unlike with sines and cosines.

Naturally, the Fourier components of the timing residual correlation, or the covariance matrix $\mathbf{\Sigma}$ [Eqs. (32) or (72)], can be expressed in terms of $\langle\psi_j(\hat{e}_a)\psi_k^*(\hat{e}_b)\rangle$. It can be shown that

$$\begin{aligned}\alpha_0(\hat{e})/2&=\psi_0(\hat{e}),\\ \alpha_k(\hat{e})&=i(\psi_k(\hat{e})-\psi_k^*(\hat{e}))(-1)^k,\\ \beta_k(\hat{e})&=(\psi_k(\hat{e})+\psi_k^*(\hat{e}))(-1)^k.\end{aligned} \tag{A9}$$

The factor $(-1)^k$ is due to shifting the time coordinate $t\to t'=t-T/2$ to match the origins of Eqs. (1) and (A4). Following the notation in the main text, we obtain

$$\begin{aligned}\frac{\langle\alpha_{aj}\alpha_{bk}\rangle}{2(-1)^{j+k}}&=\mathrm{Re}[\langle\psi_{aj}\psi_{bk}^*\rangle]-\mathrm{Re}[\langle\psi_{aj}\psi_{b(-k)}^*\rangle],\\ \frac{\langle\beta_{aj}\beta_{bk}\rangle}{2(-1)^{j+k}}&=\mathrm{Re}[\langle\psi_{aj}\psi_{bk}^*\rangle]+\mathrm{Re}[\langle\psi_{aj}\psi_{b(-k)}^*\rangle],\\ \frac{\langle\alpha_{aj}\beta_{bk}\rangle}{2(-1)^{j+k}}&=-\mathrm{Im}[\langle\psi_{aj}\psi_{bk}^*\rangle]-\mathrm{Im}[\langle\psi_{aj}\psi_{b(-k)}^*\rangle],\\ \frac{\langle\beta_{aj}\alpha_{bk}\rangle}{2(-1)^{j+k}}&=\mathrm{Im}[\langle\psi_{aj}\psi_{bk}^*\rangle]-\mathrm{Im}[\langle\psi_{aj}\psi_{b(-k)}^*\rangle].\end{aligned} \tag{A10}$$

Then, it is straightforward to confirm that the transfer functions of Eq. (1) (Secs. III C and V E) can be derived from the symmetric transfer function of Eq. (A4) [Eq. (A8)] as

$$\mathcal{C}^{\alpha}_{j,k}(f) = 2(-1)^{j+k}\left(\frac{C_{j,k}(f)+C_{-j,-k}(f)}{2} - \frac{C_{j,-k}(f)+C_{-j,k}(f)}{2}\right) = \frac{4(-1)^{j+k}f_j f_k}{(f+f_j)(f+f_k)}C_{j,k}(f),$$
$$\mathcal{C}^{\beta}_{j,k}(f) = 2(-1)^{j+k}\left(\frac{C_{j,k}(f)+C_{-j,-k}(f)}{2} + \frac{C_{j,-k}(f)+C_{-j,k}(f)}{2}\right) = \frac{4(-1)^{j+k}f^2}{(f+f_j)(f+f_k)}C_{j,k}(f),$$
$$\mathcal{C}^{\alpha\beta}_{j,k}(f) = -2(-1)^{j+k}\left(\frac{C_{j,k}(f)-C_{-j,-k}(f)}{2} + \frac{C_{j,-k}(f)-C_{-j,k}(f)}{2}\right) = -\frac{4(-1)^{j+k}f_j f}{(f+f_j)(f+f_k)}C_{j,k}(f),$$
$$\mathcal{C}^{\beta\alpha}_{j,k}(f) = 2(-1)^{j+k}\left(\frac{C_{j,k}(f)-C_{-j,-k}(f)}{2} - \frac{C_{j,-k}(f)-C_{-j,k}(f)}{2}\right) = \frac{4(-1)^{j+k}f f_k}{(f+f_j)(f+f_k)}C_{j,k}(f). \tag{A11}$$

The above relations establish the equivalence and give a dictionary to translate between Eq. (1) or Eq. (A4) when interpreting a signal in the Fourier domain.

As a consequence, the variance of the sine- and cosine-Fourier coefficients of the time correlated process is shown to be different, due to $C^{\alpha}_{j,k}(f) \neq C^{\beta}_{j,k}(f)$ (see (27) for the exact relation). To realize this, consider a very narrow signal in frequency space. In the extreme infinitesimally narrow limit, we have $I(f) \sim \delta(f-\bar{f})$. Then, the variances of the sine- and cosine-Fourier coefficients will be related to each other by $\mathrm{Var}[\beta_k^2]/\mathrm{Var}[\alpha_k^2] \sim \bar{f}^2/f_k^2$.

We now specialize back to PTA science; where the intensity of the signal can be associated with $\langle\alpha_{aj}\alpha_{bk}\rangle$ and $\langle\beta_{aj}\beta_{bk}\rangle$, and the circular polarization to $\langle\alpha_{aj}\beta_{bk}\rangle$ and $\langle\beta_{aj}\alpha_{bk}\rangle$. The above expressions make it transparent that the intensity of a signal can be associated with the real part of $\langle\psi_{aj}\psi^*_{bk}\rangle$ and the circular polarization to the imaginary part of $\langle\psi_{aj}\psi^*_{bk}\rangle$. In other words, a circularly polarized SGWB signal in a PTA can be identified either by $\langle\alpha_{aj}\beta_{bk}\rangle \neq 0$ in the sine-cosine basis (1) or $\mathrm{Im}\,[\langle\psi_{aj}\psi^*_{bk}\rangle] \neq 0$ in the exponential basis (A4).

APPENDIX B: SPIN-WEIGHTED SPHERICAL HARMONICS

The explicit form of the spin-weighted spherical harmonics that we use is

$${}_sY_{\ell m}(\theta,\phi) = (-1)^m e^{im\phi}\sqrt{\frac{(2\ell+1)}{(4\pi)}\frac{(\ell+m)!(\ell-m)!}{(\ell+s)!(\ell-s)!}} \times \sin^{2\ell}\left(\frac{\theta}{2}\right)\sum_r \binom{\ell-s}{r}\binom{\ell+s}{r+s-m} \times (-1)^{\ell-r-s}\cot^{2r+s-m}\left(\frac{\theta}{2}\right). \tag{B1}$$

When $s=0$, it reduces to the ordinary spherical harmonics,

$$Y_{\ell m}(\hat{n}) = \sqrt{\frac{(2\ell+1)}{(4\pi)}\frac{(\ell-m)!}{(\ell+m)!}}P^m_\ell(\cos\theta)e^{im\phi}. \tag{B2}$$

Spin-weighted spherical harmonics satisfy the orthogonal relation,

$$\int_{S^2} d\hat{n}\,{}_sY^*_{\ell m}(\hat{n})\,{}_sY_{\ell' m'}(\hat{n}) = \delta_{\ell\ell'}\delta_{mm'}, \tag{B3}$$

and the completeness relation,

$$\sum_{\ell m}{}_sY^*_{\ell m}(\hat{n})\,{}_sY_{\ell m}(\hat{n}') = \delta(\hat{n}-\hat{n}') = \delta(\phi-\phi')\delta(\cos\theta-\cos\theta'). \tag{B4}$$

Its complex conjugate is

$${}_sY^*_{\ell m}(\hat{n}) = (-1)^{s+m}\,{}_{-s}Y_{\ell -m}(\hat{n}), \tag{B5}$$

and its parity is given by

$${}_sY_{\ell m}(-\hat{n}) \equiv {}_sY_{\ell m}(\pi-\theta,\phi+\pi) = (-1)^\ell\,{}_{-s}Y_{\ell m}(\hat{n}). \tag{B6}$$

Also, we have the spherical wave expansion

$$e^{i\vec{k}\cdot\vec{r}} = 4\pi\sum_{\ell=0}^{\infty}\sum_{m=-\ell}^{\ell} i^\ell j_\ell(kr)Y^*_{\ell m}(\hat{k})Y_{\ell m}(\hat{r}), \tag{B7}$$

where $j_\ell(x)$ is the spherical Bessel function.

We can calculate the integral of a product of three spin-weighted spherical harmonics using the formula

$$\int_{S^2} d\hat{e}\,{}_{s_1}Y_{\ell_1 m_1}(\hat{e})\,{}_{s_2}Y_{\ell_2 m_2}(\hat{e})\,{}_{s_3}Y_{\ell_3 m_3}(\hat{e}) = \sqrt{\frac{(2\ell_1+1)(2\ell_2+1)(2\ell_3+1)}{4\pi}} \times \begin{pmatrix}\ell_1 & \ell_2 & \ell_3\\ -s_1 & -s_2 & -s_3\end{pmatrix}\begin{pmatrix}\ell_1 & \ell_2 & \ell_3\\ m_1 & m_2 & m_3\end{pmatrix}, \tag{B8}$$

which involves two Wigner-3j symbols representing the coupling coefficients between different spherical harmonics [170]. The Wigner-3j symbol is zero unless it satisfies: ℓ_1, ℓ_2, and ℓ_3 have to meet the triangular condition, i.e. $\ell_1+\ell_2 \geq \ell_3 \geq |\ell_1-\ell_2|$, while $m_1+m_2+m_3=0$; when $m_1=m_2=m_3=0$, $\ell_1+\ell_2+\ell_3$ is even. The Wigner-3j symbols have the reflection property and the summation relation

$$\begin{aligned}&\begin{pmatrix}\ell_1 & \ell_2 & \ell_3\\ s_1 & s_2 & s_3\end{pmatrix}\\&\quad=(-1)^{\ell_1+\ell_2+\ell_3}\begin{pmatrix}\ell_1 & \ell_2 & \ell_3\\ -s_1 & -s_2 & -s_3\end{pmatrix}\\&\quad=(-1)^{\ell_1+\ell_2+\ell_3}\begin{pmatrix}\ell_1 & \ell_3 & \ell_2\\ s_1 & s_3 & s_2\end{pmatrix},\end{aligned}\tag{B9}$$

$$\begin{aligned}&(2\ell+1)\sum_{m_1m_2}\begin{pmatrix}\ell & \ell_1 & \ell_2\\ m & -m_1 & m_2\end{pmatrix}\begin{pmatrix}\ell' & \ell_1 & \ell_2\\ m' & -m_1 & m_2\end{pmatrix}\\&\quad=\delta_{\ell\ell'}\delta_{mm'}.\end{aligned}\tag{B10}$$

APPENDIX C: PULSAR TIMING RESIDUALS DUE TO A GAUSSIAN SGWB SIGNAL

The pulsar timing residual simulation of PTAfast is a fork of the open-source FAKEPTA [171]. The original FAKEPTA was designed to simulate postfit pulsar timing residuals due to various astrophysical signals, including the SGWB. The pulsar, time-of-arrival generation, and noise modules of FAKEPTA are carried over to PTAfast. This includes but not limited to the Pulsar class (consisting of a simulated pulsar's position, distance, and noise properties) and functions for distributing pulsars across the sky (isotropic or anisotropic), generating time-of-arrival data, and simulating intrinsic pulsar white and colored noises.

PTAfast repurposes this as a tool for simulating prefit pulsar timing residuals with a precise and efficient SGWB signal modeling in a finite time window. Modifications of PTAfast are focused on the generation of pulsar timing residuals in a finite observation window due to a Gaussian SGWB signal.

We define the SGWB signal by its continuous support in the frequency domain, i.e., the frequency range of the SGWB signal, $f\in(f_{\rm min},f_{\rm max})$, and its power spectral density. For simplicity, we assume a power-law power spectral density (33). Then, the amplitude of the SGWB signal is given by $A_{\rm gw}$, and the spectral index is given by $\gamma_{\rm gw}$.

Once a set of pulsar objects are created, for each frequency bin, a timing data is generated as Eq. (1) where the vector of Fourier coefficients, $\boldsymbol{\alpha}$ and $\boldsymbol{\beta}$, are obtained as follows. First, we draw a vector $\boldsymbol{\xi}\sim\mathcal{N}(0,1)$ with length $2n_{\rm psrs}$ where $n_{\rm psrs}$ is the length of both $\boldsymbol{\alpha}$ and $\boldsymbol{\beta}$. We spatially correlate the pulsars according to Eqs. (28)–(29) and Eqs. (22)–(26) by constructing the covariance matrix $\boldsymbol{\Sigma}$, generally,

$$\Sigma^{jk}_{ab}\equiv\begin{pmatrix}\langle\alpha_{aj}\alpha_{bk}\rangle & \langle\alpha_{aj}\beta_{bk}\rangle\\ \langle\beta_{aj}\alpha_{bk}\rangle & \langle\beta_{aj}\beta_{bk}\rangle\end{pmatrix},\tag{C1}$$

for all pulsar pairs (a,b) and frequency bins j, k. For a fixed frequency bin k, the covariance matrix $\boldsymbol{\Sigma}$ is a $2n_{\rm psrs}\times 2n_{\rm psrs}$ matrix. The Fourier components of the correlation such as $\langle\alpha_{aj}\alpha_{bk}\rangle$ and $\langle\beta_{aj}\beta_{bk}\rangle$ are computed by convolving the transfer functions (22)–(26) with the power spectral density across the support of the signal. Finally, the input Fourier coefficients $\boldsymbol{\alpha}$ and $\boldsymbol{\beta}$ are obtained as $\boldsymbol{\alpha},\boldsymbol{\beta}\sim\mathbf{L}\boldsymbol{\xi}$ where $\mathbf{L}$ is the lower triangular matrix of the Cholesky decomposition of the covariance matrix $\boldsymbol{\Sigma}$, i.e., $\boldsymbol{\Sigma}\equiv\mathbf{L}\mathbf{L}^{\rm T}$. See also Appendix C of [130].

Simulated pulsar timing residuals following the above prescription are shown in Fig. 2. In this case, we consider a power law power spectrum (33) and the Hellings-Downs curve $\Gamma^{\rm HD}(\hat{e}_a\cdot\hat{e}_b)=(1+\delta_{ab})\mathbf{\Gamma}(f)$ for the spatial correlation. This corresponds to an unpolarized SGWB signal; with a continuous support in $f\in(1,100)$ nHz. Then, the nontrivial elements of the covariance matrix are given by

$$\langle\alpha_{aj}\alpha_{bk}\rangle=\Gamma^{\rm HD}(\hat{e}_a\cdot\hat{e}_b)\int_{f_{\rm min}}^{f_{\rm max}}dfS(f)\mathcal{C}^{\alpha}_{j,k}(f)\tag{C2}$$

and

$$\langle\beta_{aj}\beta_{bk}\rangle=\Gamma^{\rm HD}(\hat{e}_a\cdot\hat{e}_b)\int_{f_{\rm min}}^{f_{\rm max}}dfS(f)\mathcal{C}^{\beta}_{j,k}(f),\tag{C3}$$

where $f_{\rm min}=1$ nHz and $f_{\rm max}=100$ nHz. Note that we have pulled out the HD curve, $\Gamma^{\rm HD}(\hat{e}_a\cdot\hat{e}_b)$, out of the integral. Also, $\langle\alpha_{aj}\beta_{bk}\rangle=\langle\beta_{aj}\alpha_{bk}\rangle=0$ for an unpolarized SGWB signal.

For comparison, pulsar timing data simulations with and without transfer functions as well as with and without white noise are presented in Fig. 2. Three representative pulsars are shown. For white noise, we draw the usual pulsar noise parameters EFAC, EQUAD, and ECORR [171] from a uniform distribution, i.e., EFAC $\sim U(0.8,1.1)$, EQUAD $\sim U(-8,-6)$, and ECORR $\sim U(-8,-6)$. The white noise is added to the simulated residuals after the SGWB signal is generated. Generally, a white noise component is uncorrelated in time and frequency, and across pulsars. This is the case with EFAC and EQUAD. As a special case, ECORR is associated to pulsar jitter noise which is correlated across frequency subbands.

Figure 2 demonstrates that the SGWB signal is clearly visible in the timing residuals, even when white noise is present. However, the inclusion of transfer functions is crucial for accurately capturing the high-frequency features of the SGWB in the residuals, as illustrated by the differences

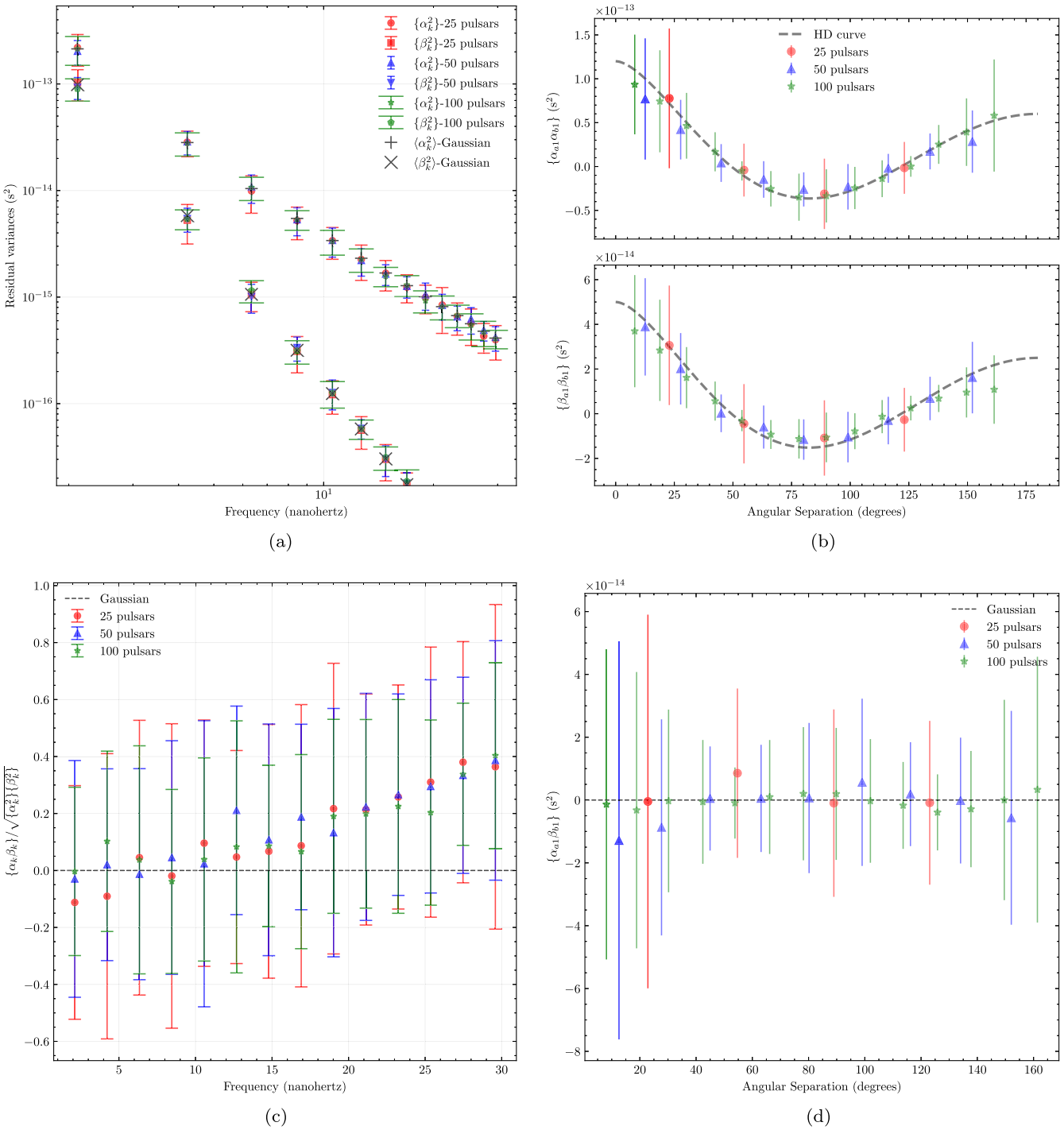


FIG. 7. Fourier components of timing residual correlation due to a Gaussian SGWB signal for different number of pulsars in 15-year PTAfast simulations: (a) sample variances, (b) two-point correlation function, (c) cross-Fourier statistic $\{\alpha_k\beta_k\}/\sqrt{\{\alpha_k^2\}\{\beta_k^2\}}$, and (d) cross-Fourier spatial correlation $\{\alpha_{a1}\beta_{b1}\}$. Red, blue, and green points refer to 25, 50, and 100 pulsars, respectively, and the error bars represent the standard error across 50 realizations. Black points and dashed curves show the Gaussian theoretical expectation values based on Eqs. (28)–(29) and Eqs. (22)–(26).

between the top and bottom panels of Fig. 2. At higher levels of white noise, these high-frequency components can be obscured. Moreover, transfer functions are essential for recovering the correct amplitude of the SGWB signal: without them, the simulated residuals have amplitudes roughly half those obtained when transfer functions are included. Notably, the implementation with transfer functions yields SGWB signal amplitudes and statistics that are in agreement with those produced by direct superposition of gravitational waves from individual sources [117,126].

APPENDIX D: NUMBER OF PULSARS

We present results complementary to Sec. IV for varying number of pulsars in Fig. 7.

The number of pulsar pairs for a $n_{\rm psrs}$ array is given by $n_{\rm psrs}(n_{\rm psrs}-1)/2$. The number of pulsar pairs is important for the significance of the SGWB signal in a realization. In Fig. 7, we show the Fourier components of timing residual correlation due to a Gaussian SGWB signal for different number of pulsars in 15-year PTAfast simulations. The results are shown for 25, 50, and 100 pulsars, respectively. The error bars represent the standard error across 50 realizations. The black points and dashed curves show the Gaussian theoretical expectation values based on Eqs. (28)–(29) and Eqs. (22)–(26). See Appendix C for details on the simulation procedure.

All cases are consistent with the theoretical expectation values of the variances and the Hellings-Downs curve. However, the size of the ensemble variances (visible as error bars in Fig. 7) depends on the number of pulsars in the array. With more pulsars, there are more independent pulsar pairs contributing to each angular bin, which improves the statistical sampling and reduces the variance across different realizations. As a result, the error bars shrink as the number of pulsars increases. In the limit of a very large array ($n_{\rm psrs}\to\infty$), the ensemble variance approaches the cosmic variance [101,160–162]. For a finite array, the SGWB signal in a given realization can deviate from the theoretical mean by down to the cosmic variance, but increasing the number of pulsars systematically reduces this variation, as seen in Fig. 7.

APPENDIX E: QUICK RECIPE FOR COMPUTING THE ELEMENTS OF THE COVARIANCE MATRIX

We put together formulas for computing the elements of the covariance matrix in the frequency- and Fourier-domain (Sec. II).

For an *unpolarized* SGWB, the relevant Fourier components of the correlation are given by

$$\langle\alpha_{aj}\alpha_{bk}\rangle=\mathcal{F}\left[\sum_{\ell m}I_{\ell m}(f)\gamma^{I}_{\ell m}(fD_a,fD_b,\hat{e}_a,\hat{e}_b),\mathcal{C}^{\alpha}_{j,k}(f)\right], \tag{E1}$$

and

$$\langle\beta_{aj}\beta_{bk}\rangle=\mathcal{F}\left[\sum_{\ell m}I_{\ell m}(f)\gamma^{I}_{\ell m}(fD_a,fD_b,\hat{e}_a,\hat{e}_b),\mathcal{C}^{\beta}_{j,k}(f)\right], \tag{E2}$$

where the functional $\mathcal{F}$ is defined as

$$\mathcal{F}[G(f,y),\mathcal{C}(f)]=\int_{f_{\rm min}}^{f_{\rm max}}\frac{2df}{(2\pi f)^2}G(f,y)\mathcal{C}(f), \tag{E3}$$

and $\mathcal{C}^{\alpha/\beta}_{j,k}(f)$ are given by

$$\mathcal{C}^{\alpha}_{j,k}(f)=\frac{4f_jf_k}{\pi^2T^2}\frac{\sin^2(\pi fT)}{(f^2-f_j^2)(f^2-f_k^2)}, \tag{E4}$$

$$\mathcal{C}^{\beta}_{j,k}(f)=\frac{4f^2}{\pi^2T^2}\frac{\sin^2(\pi fT)}{(f^2-f_j^2)(f^2-f_k^2)}. \tag{E5}$$

For a *circularly polarized* SGWB, the relevant Fourier components of the correlation pertaining to circular polarization are given by

$$\langle\alpha_{aj}\beta_{bk}\rangle=\mathcal{F}\left[\sum_{\ell m}iV_{\ell m}(f)\gamma^{V}_{\ell m}(fD_a,fD_b,\hat{e}_a,\hat{e}_b),\mathcal{C}^{\alpha\beta}_{j,k}(f)\right], \tag{E6}$$

where $\mathcal{C}^{\alpha\beta}_{j,k}(f)$ are given by

$$\mathcal{C}^{\alpha\beta}_{j,k}(f)=-\frac{4f_jf}{\pi^2T^2}\frac{\sin^2(\pi fT)}{(f^2-f_j^2)(f^2-f_k^2)},$$
$$\mathcal{C}^{\beta\alpha}_{j,k}(f)=\frac{4f_kf}{\pi^2T^2}\frac{\sin^2(\pi fT)}{(f^2-f_j^2)(f^2-f_k^2)}. \tag{E7}$$

The $I_{lm}(f)$'s and $V_{lm}(f)$'s are spherical harmonic components of the Stokes parameters of the SGWB power spectra. The overlap reduction functions (ORFs) $\gamma^{X}_{lm}(f,x)$'s can be calculated as described in Refs. [100,131] or in the computational frame [128,130] using PTAfast [143,156,157,162].

APPENDIX F: STANDARD ERRORS OF THE KINEMATIC DIPOLE CORRELATIONS

The results of simulations of a circularly polarized PTA signal in Sec. VI or Fig. 6 with standard errors are shown in Fig. 8. The standard errors SE are related to the standard error on the mean SEM via $\mathrm{SEM}=\mathrm{SE}/\sqrt{n_{\rm reals}}$ where $n_{\rm reals}$ is the number of independent realizations of an experiment or a simulation. The SEM is useful for highlighting the existence of a signal, since it can be reduced indefinitely by increasing the number of independent realizations. On the other hand, standard errors are representative of the variation across realizations for multiple repeated simulations of an experiment.

APPENDIX G: THE ANISOTROPIC UNPOLARIZED SIGNAL

It might be instructive to look at the anisotropic unpolarized case, in addition to the anisotropic and

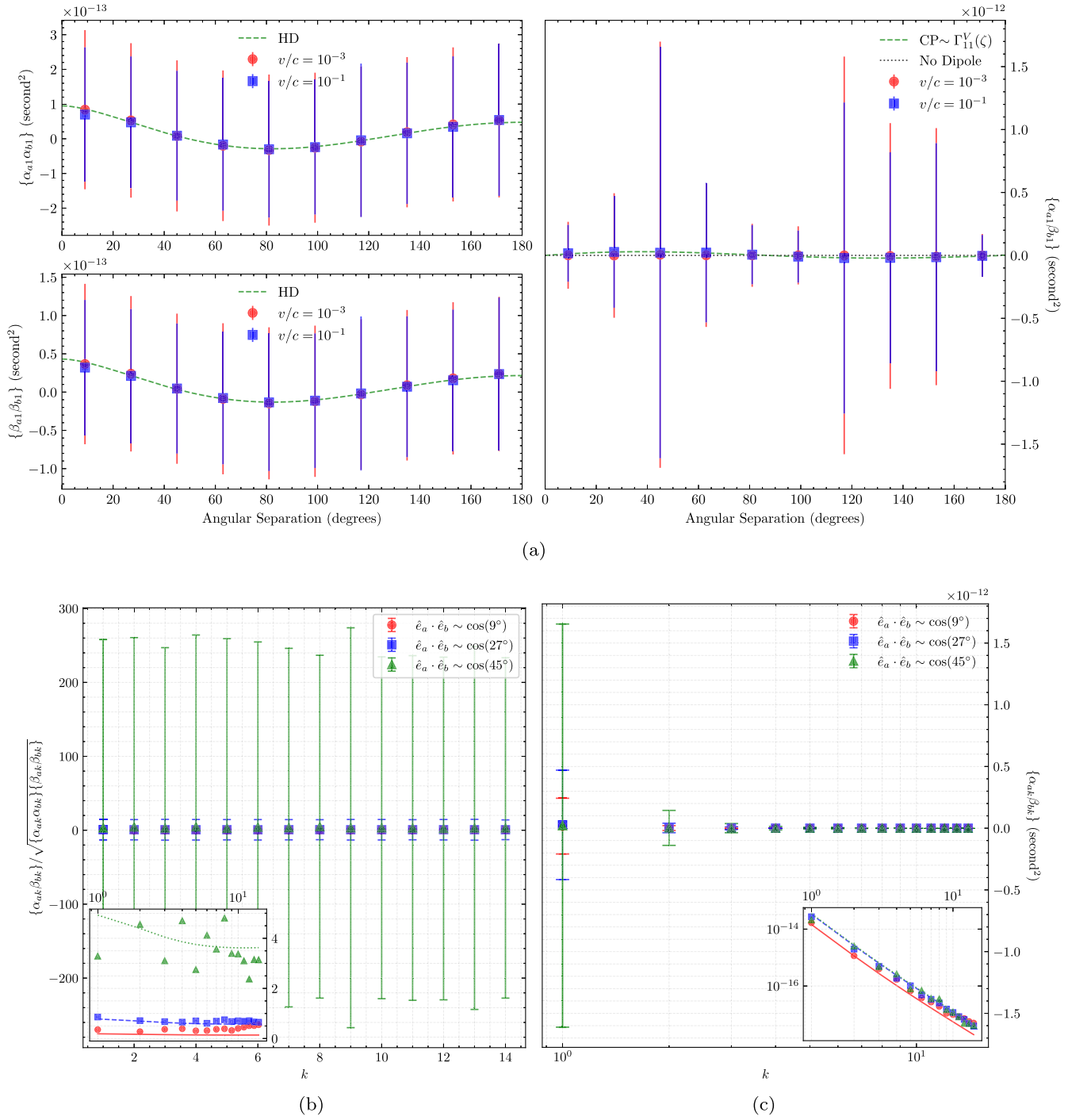


FIG. 8. Top panel: two-point correlation functions and bottom panel: the bin power of the Fourier coefficients of pulsar timing residuals for a simulated 15-year PTA dataset with a circularly polarized SGWB signal. The parameters are exactly the same as Fig. 6, except the error bars shown are the standard errors (variations across realizations); the inset plots at the bottom panel show the means. In the top panel, the green dashed lines are the theoretical expectation values. In the insets of the bottom panel, the colored curves (red-solid, blue-dashed, and green-dotted) represent the theoretical expectation values of the frequency-bin power of the cross-Fourier statistic $\{\alpha_{ak}\beta_{bk}\}$ at $9°, 27°, 45°$ angular bins.

circularly polarized one presented in the main text. These were generated as a special case of the methodology discussed in the main text, simply by setting $V_{00}(f) = 0$ or $\Pi = 0$ (zero circular polarization); the relevant corrections to the correlation appear in (73) or (60) whereas the terms that are contained in(74) or (61) reduce to zero with $\Pi = 0$. In this case, sines and cosines will be uncorrelated, and so we may focus on the sample averages

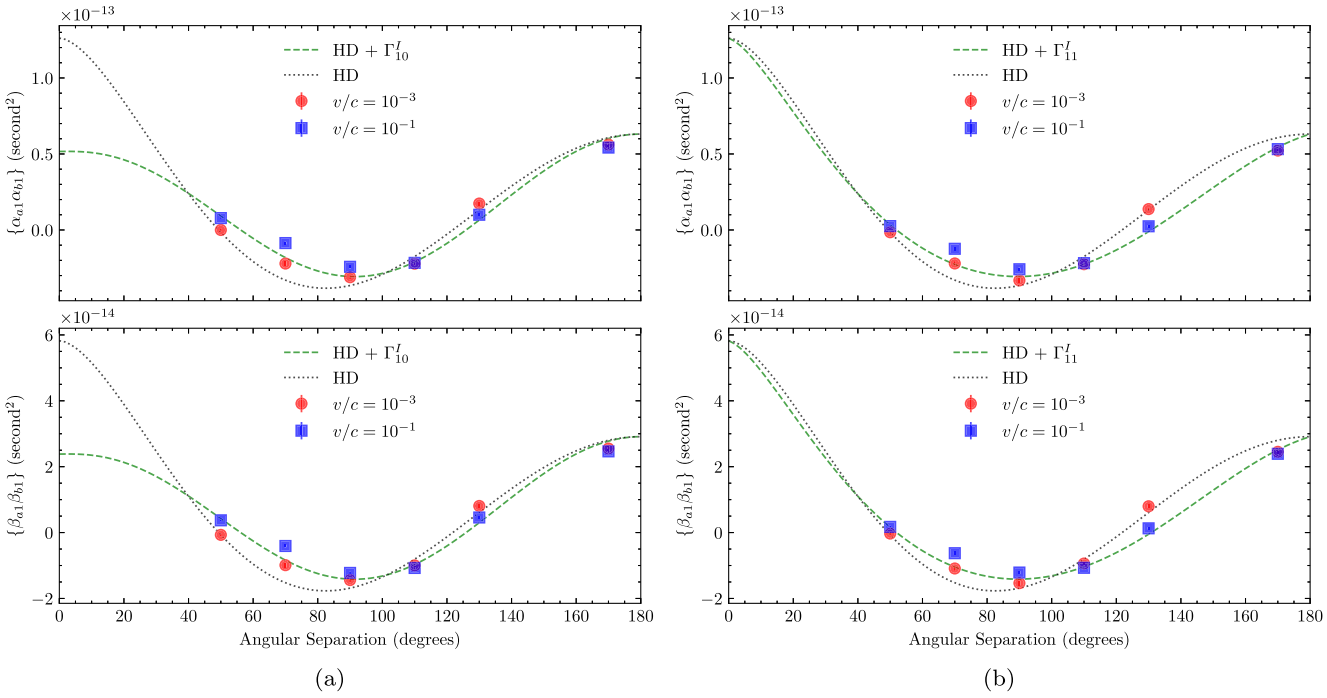


FIG. 9. Correlation functions in the purely anisotropic case with (a) Γ^I_{10} and (b) Γ^I_{11} in simulated 15-year PTA data. HD + Γ^I_{10} and HD + Γ^I_{11} in the legends are shorthand for the full terms in (73) or (60); with kinematic dipole speeds $\beta = v/c = 10^{-3}$ (round points) and 10^{-1} (square points). Each of 20000 realizations has 10 pulsars at fixed positions; in (a) these are arranged so that $\cos(\theta_v) = 1$, $\sin(\theta_v) = 0$, in (b) $\cos(\theta_v) = 0$, $\sin(\theta_v) = \cos(\phi_v) = 1$. The error bars are the error on the mean. The SGWB strain and spectral index are $A_{\rm gw} = 10^{-15}$ and $\gamma_{\rm gw} = 13/3$, respectively. The green dashed lines represent the Gaussian theoretical expectation values and the dotted line is the HD curve.

$\{\alpha_{ak}\alpha_{bk}\}$ and $\{\beta_{ak}\beta_{bk}\}$ in each realization. The results in the first frequency bin with a SGWB characteristic strain $A_{\rm gw} = 10^{-15}$, spectral index $\gamma_{\rm gw} = 13/3$, kinematic dipole speeds $v/c = 10^{-3}$ and 10^{-1} are shown in Fig. 9. For this set of simulations, in each realization, a mock 15-year PTA data with 10 pulsars at fixed positions are generated. A total of 20000 realizations were considered.

The reason for considering 10 pulsars and 20000 realizations is the following. Two anisotropic corrections [$\mathcal{O}(v/c)$ terms in (73) or (60)] with distinct computational frame ORFs ($\mathbf{\Gamma}^I_{10}(\hat{e}_a \cdot \hat{e}_b)$ and $\mathbf{\Gamma}^I_{11}(\hat{e}_a \cdot \hat{e}_b)$ trail the HD curve in the sine-sine and cosine-cosine correlations). Thus, to look into each one, rather than both at the same time, we utilized pulsars that are in a very specific configuration relative to the direction of the kinematic dipole. In particular, to obtain the HD correlation plus the leading anisotropic $\mathbf{\Gamma}^I_{10}(\hat{e}_a \cdot \hat{e}_b)$ correction, we considered a pulsar-dipole configuration with $\cos(\theta_v) = 1$, $\sin(\theta_v) = 0$ (pulsars on the plane of the dipole and pulsar a). For the $\mathbf{\Gamma}^I_{11}(\hat{e}_a \cdot \hat{e}_b)$ correction, we considered $\cos(\theta_v) = 0$, $\sin(\theta_v) = \cos(\phi_v) = 1$ (dipole and pulsar a point to the same direction whereas the rest of the pulsars lie on a plane). However, these specific configurations correspond to pulsars that lie on a plane instead of scattered anisotropically. In a fixed frame, points that are uniformly distributed on the two-sphere follow a distribution function $(\sin\theta)/2$, and that the fraction that would be on a plane (e.g., positive xz plane) will be $\sin(\Delta\theta/2)$ where $\Delta\theta$ is a resolution. With an angular resolution of a degree, this fraction is approximately $\sin(\pi/360) \sim 0.009$. Should there be a 1000 pulsars that are distributed uniformly, then around 10 can be expected to lie on any fixed plane given a one-degree resolution. Then we utilize only 10 pulsars based on this rough estimate to simulate the anisotropic corrections with correlation functions $\mathbf{\Gamma}^I_{10}(\hat{e}_a \cdot \hat{e}_b)$ and $\mathbf{\Gamma}^I_{11}(\hat{e}_a \cdot \hat{e}_b)$. To confront the limited sample statistics with a small number of pulsars, we have increased the number of realizations to 20000, which is twice compared to that used throughout the main text.

Figure 9 shows that both anisotropic correlations $\mathbf{\Gamma}^I_{10}(\hat{e}_a \cdot \hat{e}_b)$ and $\mathbf{\Gamma}^I_{11}(\hat{e}_a \cdot \hat{e}_b)$ are recovered consistently in simulations when the dipole's speed is artificially increased to $v/c = 10^{-1}$ (a tenth of the speed of light). When the dipole speed is $v/c = 10^{-3}$, the results reduce to the HD correlation. It must be mentioned that because there are only ten pulsars that there are only nine pulsar pairs in a frame dependent search, and fewer angular bins. Arguably, the results with anisotropy are expected to be challenging to distinguish to the HD curve even when the dipole's speed has already been increased unrealistically; again, this is

because the terms are suppressed by v/c relative to the HD curve in the sine-sine and cosine-cosine correlations. This is one reason we preferred to focus on circular polarization in the main text, because the dipole signal of circular polarization alone correlates the sine and cosine coefficients.

[1] Gabriella Agazie *et al.* (NANOGrav Collaboration), The NANOGrav 15 yr data set: Evidence for a gravitational-wave background, Astrophys. J. Lett. **951**, L8 (2023).

[2] Daniel J. Reardon *et al.*, Search for an isotropic gravitational-wave background with the parkes pulsar timing array, Astrophys. J. Lett. **951**, L6 (2023).

[3] J. Antoniadis *et al.* (EPTA and InPTA Collaborations), The second data release from the European Pulsar Timing Array—III. Search for gravitational wave signals, Astron. Astrophys. **678**, A50 (2023).

[4] Heng Xu *et al.*, Searching for the nano-hertz stochastic gravitational wave background with the Chinese pulsar timing array data release I, Res. Astron. Astrophys. **23**, 075024 (2023).

[5] Matthew T. Miles *et al.*, The MeerKAT pulsar timing array: The first search for gravitational waves with the MeerKAT radio telescope, Mon. Not. R. Astron. Soc. **536**, 1489 (2025).

[6] B. P. Abbott *et al.* (LIGO Scientific and Virgo Collaborations), Observation of gravitational waves from a binary black hole merger, Phys. Rev. Lett. **116**, 061102 (2016).

[7] R. Abbott *et al.* (KAGRA, VIRGO, and LIGO Scientific Collaborations), GWTC-3: Compact binary coalescences observed by LIGO and Virgo during the second part of the third observing run, Phys. Rev. X **13**, 041039 (2023).

[8] R. Abbott *et al.* (LIGO Scientific, VIRGO, and KAGRA Collaborations), Tests of general relativity with GWTC-3, Phys. Rev. D **112**, 084080 (2025).

[9] Bhal Chandra Joshi, Pulsar timing arrays, Int. J. Mod. Phys. D **22**, 1341008 (2013).

[10] Maura McLaughlin, The international pulsar timing array: A galactic scale gravitational wave observatory, Gen. Relativ. Gravit. **46**, 1810 (2014).

[11] R. N. Manchester, Pulsars and Gravity, Int. J. Mod. Phys. D **24**, 1530018 (2015).

[12] Andrea N. Lommen, Pulsar timing arrays: The promise of gravitational wave detection, Rep. Prog. Phys. **78**, 124901 (2015).

[13] Joseph D. Romano and Neil J. Cornish, Detection methods for stochastic gravitational-wave backgrounds: A unified treatment, Living Rev. Relativity **20**, 2 (2017).

[14] Werner Becker, Michael Kramer, and Alberto Sesana, Pulsar timing and its application for navigation and gravitational wave detection, Space Sci. Rev. **214**, 30 (2018).

[15] J. P. W. Verbiest, S. Osłowski, and S. Burke-Spolaor, Pulsar timing array experiments, in *Handbook of Gravitational Wave Astronomy*, edited by Cosimo Bambi, Stavros Katsanevas, and Konstantinos D. Kokkotas (Springer, Singapore, 2021), p. 4.

[16] Stephen R. Taylor, The nanohertz gravitational wave astronomer, arXiv:2105.13270.

[17] Joris P. W. Verbiest, Sarah J. Vigeland, Nataliya K. Porayko, Siyuan Chen, and Daniel J. Reardon, Status report on global pulsar-timing-array efforts to detect gravitational waves, Results Phys. **61**, 107719 (2024).

[18] Nicolas Yunes, Xavier Siemens, and Kent Yagi, Gravitational-wave tests of general relativity with ground-based detectors and pulsar-timing arrays, arXiv:2408.05240.

[19] Valerie Domcke, Discovery opportunities with gravitational waves—TASI 2024 lecture notes, arXiv:2409.08956.

[20] Chiara Caprini and Daniel G. Figueroa, Cosmological backgrounds of gravitational waves, Classical Quantum Gravity **35**, 163001 (2018).

[21] Nelson Christensen, Stochastic gravitational wave backgrounds, Rep. Prog. Phys. **82**, 016903 (2019).

[22] Joseph D. Romano, Searches for stochastic gravitational-wave backgrounds, arXiv:1909.00269.

[23] Christopher J. Moore and Alberto Vecchio, Ultra-low-frequency gravitational waves from cosmological and astrophysical processes, Nat. Astron. **5**, 1268 (2021).

[24] Nihan S. Pol *et al.* (NANOGrav Collaboration), Astrophysics milestones for pulsar timing array gravitational-wave detection, Astrophys. J. Lett. **911**, L34 (2021).

[25] Nihan Pol, Stephen R. Taylor, and Joseph D. Romano, Forecasting pulsar timing array sensitivity to anisotropy in the stochastic gravitational wave background, Astrophys. J. **940**, 173 (2022).

[26] Seppe Staelens and Gijs Nelemans, Likelihood of white dwarf binaries to dominate the astrophysical gravitational wave background in the mHz band, Astron. Astrophys. **683**, A139 (2024).

[27] Yifan Chen, Yuxiang Liu, Jing Shu, Bin Xu, Xiao Xue, and Yanjie Zeng, Identifying the quadrupolar nature of gravitational wave background through space-based missions, J. Cosmol. Astropart. Phys. 08 (2025) 063.

[28] Mikhail V. Sazhin, Opportunities for detecting ultralong gravitational waves, Sov. Astron. **22**, 36 (1978), https://articles.adsabs.harvard.edu/pdf/1978SvA....22...36S.

[29] Steven L. Detweiler, Pulsar timing measurements and the search for gravitational waves, Astrophys. J. **234**, 1100 (1979).

[30] E. S. Phinney, A practical theorem on gravitational wave backgrounds, arXiv:astro-ph/0108028.

[31] J. Stuart B. Wyithe and Abraham Loeb, Low—frequency gravitational waves from massive black hole binaries: Predictions for LISA and pulsar timing arrays, Astrophys. J. **590**, 691 (2003).

[32] Alberto Sesana, Francesco Haardt, Piero Madau, and Marta Volonteri, Low—frequency gravitational radiation

from coalescing massive black hole binaries in hierarchical cosmologies, Astrophys. J. **611**, 623 (2004).
[33] Alberto Sesana, Alberto Vecchio, and Carlo Nicola Colacino, The stochastic gravitational-wave background from massive black hole binary systems: Implications for observations with Pulsar Timing Arrays, Mon. Not. R. Astron. Soc. **390**, 192 (2008).
[34] Sarah J. Vigeland and Xavier Siemens, Supermassive black hole binary environments: Effects on the scaling laws and time to detection for the stochastic background, Phys. Rev. D **94**, 123003 (2016).
[35] Sarah Burke-Spolaor *et al.*, The astrophysics of nanohertz gravitational waves, Astron. Astrophys. Rev. **27**, 5 (2019).
[36] Tingting Liu and Sarah J. Vigeland, Multi-messenger approaches to supermassive black hole binary detection and parameter estimation: Implications for nanohertz gravitational wave searches with pulsar timing arrays, Astrophys. J. **921**, 178 (2021).
[37] Gabriela Sato-Polito, Matias Zaldarriaga, and Eliot Quataert, Where are NANOGrav's big black holes?, Phys. Rev. D **110**, 063020 (2024).
[38] Gabriela Sato-Polito and Marc Kamionkowski, Exploring the spectrum of stochastic gravitational-wave anisotropies with pulsar timing arrays, Phys. Rev. D **109**, 123544 (2024).
[39] Yan-Chen Bi, Yu-Mei Wu, Zu-Cheng Chen, and Qing-Guo Huang, Implications for the supermassive black hole binaries from the NANOGrav 15-year data set, Sci. China Phys. Mech. Astron. **66**, 120402 (2023).
[40] Gabriela Sato-Polito and Matias Zaldarriaga, The distribution of the gravitational-wave background from supermassive black holes, Phys. Rev. D **111**, 023043 (2025).
[41] Mohit Raj Sah, Suvodip Mukherjee, Vida Saeedzadeh, Arif Babul, Michael Tremmel, and Thomas R. Quinn, Imprints of supermassive black hole evolution on the spectral and spatial anisotropy of nano-hertz stochastic gravitational-wave background, Mon. Not. R. Astron. Soc. **533**, 1568 (2024).
[42] Juhan Raidal, Juan Urrutia, Ville Vaskonen, and Hardi Veermäe, Eccentricity effects on the SMBH GW background, Astron. Astrophys. **691**, A212 (2024).
[43] Mohit Raj Sah and Suvodip Mukherjee, Discovering the cosmic evolution of supermassive black holes using nano-Hertz gravitational waves and galaxy surveys, arXiv:2407.11669.
[44] R. W. Hellings and G. W. Downs, Upper limits on the isotropic gravitational radiation background from pulsar timing analysis, Astrophys. J. Lett. **265**, L39 (1983).
[45] Fredrick A. Jenet and Joseph D. Romano, Understanding the gravitational-wave Hellings and Downs curve for pulsar timing arrays in terms of sound and electromagnetic waves, Am. J. Phys. **83**, 635 (2015).
[46] Joseph D. Romano and Bruce Allen, Answers to frequently asked questions about the pulsar timing array Hellings and Downs curve, Classical Quantum Gravity **41**, 175008 (2024).
[47] Zu-Cheng Chen, Chen Yuan, and Qing-Guo Huang, Pulsar timing array constraints on primordial black holes with NANOGrav 11-year dataset, Phys. Rev. Lett. **124**, 251101 (2020).
[48] John Ellis and Marek Lewicki, Cosmic string interpretation of NANOGrav pulsar timing data, Phys. Rev. Lett. **126**, 041304 (2021).
[49] Sunny Vagnozzi, Implications of the NANOGrav results for inflation, Mon. Not. R. Astron. Soc. **502**, L11 (2021).
[50] Rome Samanta and Satyabrata Datta, Gravitational wave complementarity and impact of NANOGrav data on gravitational leptogenesis, J. High Energy Phys. 05 (2021) 211.
[51] Micol Benetti, Leila Lobato Graef, and Sunny Vagnozzi, Primordial gravitational waves from NANOGrav: A broken power-law approach, Phys. Rev. D **105**, 043520 (2022).
[52] Zaven Arzoumanian *et al.* (NANOGrav Collaboration), Searching for gravitational waves from cosmological phase transitions with the NANOGrav 12.5-year dataset, Phys. Rev. Lett. **127**, 251302 (2021).
[53] Wilfried Buchmuller, Valerie Domcke, and Kai Schmitz, Stochastic gravitational-wave background from metastable cosmic strings, J. Cosmol. Astropart. Phys. 12 (2021) 006.
[54] Heling Deng, Gravitational wave background from mergers of large primordial black holes, J. Cosmol. Astropart. Phys. 03 (2022) 037.
[55] Xiao Xue *et al.*, Constraining cosmological phase transitions with the parkes pulsar timing array, Phys. Rev. Lett. **127**, 251303 (2021).
[56] Ramkishor Sharma, Constraining models of inflationary magnetogenesis with NANOGrav data, Phys. Rev. D **105**, L041302 (2022).
[57] J. Antoniadis *et al.* (EPTA and InPTA Collaborations), The second data release from the European Pulsar Timing Array—IV. Implications for massive black holes, dark matter, and the early Universe, Astron. Astrophys. **685**, A94 (2024).
[58] Ido Ben-Dayan, Utkarsh Kumar, Udaykrishna Thattarampilly, and Amresh Verma, Probing the early Universe cosmology with NANOGrav: Possibilities and limitations, Phys. Rev. D **108**, 103507 (2023).
[59] Sunny Vagnozzi, Inflationary interpretation of the stochastic gravitational wave background signal detected by pulsar timing array experiments, J. High Energy Astrophys. **39**, 81 (2023).
[60] Daniel G. Figueroa, Mauro Pieroni, Angelo Ricciardone, and Peera Simakachorn, Cosmological background interpretation of pulsar timing array data, Phys. Rev. Lett. **132**, 171002 (2024).
[61] John Ellis, Malcolm Fairbairn, Gert Hütsi, Juhan Raidal, Juan Urrutia, Ville Vaskonen, and Hardi Veermäe, Gravitational waves from supermassive black hole binaries in light of the NANOGrav 15-year data, Phys. Rev. D **109**, L021302 (2024).
[62] Vida Saeedzadeh, Suvodip Mukherjee, Arif Babul, Michael Tremmel, and Thomas R. Quinn, Shining light on the hosts of the nano-Hertz gravitational wave sources: A theoretical perspective, Mon. Not. R. Astron. Soc. **529**, 4295 (2024).
[63] Lang Liu, Zu-Cheng Chen, and Qing-Guo Huang, Probing the equation of state of the early Universe with pulsar timing arrays, J. Cosmol. Astropart. Phys. 11 (2023) 071.

[64] Lang Liu, You Wu, and Zu-Cheng Chen, Simultaneously probing the sound speed and equation of state of the early Universe with pulsar timing arrays, J. Cosmol. Astropart. Phys. 04 (2024) 011.
[65] Zu-Cheng Chen, Shou-Long Li, Puxun Wu, and Hongwei Yu, NANOGrav hints for first-order confinement-deconfinement phase transition in different QCD-matter scenarios, Phys. Rev. D **109**, 043022 (2024).
[66] Lang Liu, Zu-Cheng Chen, and Qing-Guo Huang, Implications for the non-Gaussianity of curvature perturbation from pulsar timing arrays, Phys. Rev. D **109**, L061301 (2024).
[67] Jia-Heng Jin, Zu-Cheng Chen, Zhu Yi, Zhi-Qiang You, Lang Liu, and You Wu, Confronting sound speed resonance with pulsar timing arrays, J. Cosmol. Astropart. Phys. 09 (2023) 016.
[68] Hai-Long Huang, Yong Cai, Jun-Qian Jiang, Jun Zhang, and Yun-Song Piao, Supermassive primordial black holes for nano-Hertz gravitational waves and high-redshift JWST galaxies, Res. Astron. Astrophys. **24**, 091001 (2024).
[69] Gen Ye, Mian Zhu, and Yong Cai, Null energy condition violation during inflation and pulsar timing array observations, J. High Energy Phys. 02 (2024) 008.
[70] Sai Wang, Zhi-Chao Zhao, and Qing-Hua Zhu, Constraints on scalar-induced gravitational waves up to third order from a joint analysis of BBN, CMB, and PTA data, Phys. Rev. Res. **6**, 013207 (2024).
[71] Sai Wang, Zhi-Chao Zhao, Jun-Peng Li, and Qing-Hua Zhu, XImplications of pulsar timing array data for scalar-induced gravitational waves and primordial black holes: Primordial non-Gaussianity fNL considered, Phys. Rev. Res. **6**, L012060 (2024).
[72] Mian Zhu, Gen Ye, and Yong Cai, Pulsar timing array observations as possible hints for nonsingular cosmology, Eur. Phys. J. C **83**, 816 (2023).
[73] Jun-Qian Jiang, Yong Cai, Gen Ye, and Yun-Song Piao, Broken blue-tilted inflationary gravitational waves: A joint analysis of NANOGrav 15-year and BICEP/Keck 2018 data, J. Cosmol. Astropart. Phys. 05 (2024) 004.
[74] Ligong Bian, Shuailiang Ge, Jing Shu, Bo Wang, Xing-Yu Yang, and Junchao Zong, Gravitational wave sources for Pulsar Timing Arrays, Phys. Rev. D **109**, L101301 (2024).
[75] Satyabrata Datta and Rome Samanta, Fingerprints of GeV scale right-handed neutrinos on inflationary gravitational waves and PTA data, Phys. Rev. D **108**, L091706 (2023).
[76] Satyabrata Datta, Explaining PTA data with inflationary GWs in a PBH-dominated universe, J. Cosmol. Astropart. Phys. 10 (2024) 009.
[77] Debtosh Chowdhury, Arpan Hait, Subhendra Mohanty, and Suraj Prakash, Ultralight dark matter explanation of NANOGrav observations, Phys. Rev. D **110**, 083023 (2024).
[78] Jun-Qian Jiang and Yun-Song Piao, Search for the nonlinearities of gravitational wave background in NANOGrav 15-year data set, Phys. Lett. B **862**, 139284 (2025).
[79] Martin Wolfgang Winkler and Katherine Freese, Origin of the stochastic gravitational wave background: First-order phase transition vs. Black hole mergers, Phys. Rev. D **111**, 083509 (2025).
[80] Utkarsh Kumar, Udaykrishna Thattarampilly, and Pankaj Chaturvedi, Probe of spatial geometry from scalar induced gravitational waves, arXiv:2410.12931.
[81] Gabriella Agazie *et al.*, The NANOGrav 15 yr data set: Running of the spectral index, Astrophys. J. Lett. **978**, L29 (2025).
[82] Marco Calzà, Francesco Gianesello, Massimiliano Rinaldi, and Sunny Vagnozzi, Implications of cosmologically coupled black holes for pulsar timing arrays, Sci. Rep. **14**, 31296 (2024).
[83] Theodoros Papanikolaou, Shreya Banerjee, Yi-Fu Cai, Salvatore Capozziello, and Emmanuel N. Saridakis, Primordial black holes and induced gravitational waves in non-singular matter bouncing cosmology, J. Cosmol. Astropart. Phys. 06 (2024) 066.
[84] Theodoros Papanikolaou, Charalampos Tzerefos, Salvatore Capozziello, and Gaetano Lambiase, Gravitational-wave signatures of gravito-electromagnetic couplings, J. Cosmol. Astropart. Phys. 01 (2025) 051.
[85] Spyros Basilakos, Dimitri V. Nanopoulos, Theodoros Papanikolaou, Emmanuel N. Saridakis, and Charalampos Tzerefos, Observable signatures of no-scale supergravity in NANOGrav, Int. J. Mod. Phys. D **33**, 2441014 (2024).
[86] Lu Yin, Does Gauss-Bonnet inflationary gravitational waves satisfy the pulsar timing arrays observations?, J. Cosmol. Astropart. Phys. 05 (2025) 047.
[87] Satyabrata Datta and Rome Samanta, Cosmic superstrings, metastable strings and ultralight primordial black holes: From NANOGrav to LIGO and beyond, J. High Energy Phys. 02 (2025) 095.
[88] Peter Athron, Marco Chianese, Satyabrata Datta, Rome Samanta, and Ninetta Saviano, Impact of memory-burdened black holes on primordial gravitational waves in light of Pulsar Timing Array, J. Cosmol. Astropart. Phys. 05 (2025) 005.
[89] Samuel Sánchez López and José Jaime Terente Díaz, Scalar-induced gravitational waves in Palatini $f(R)$ gravity, J. Cosmol. Astropart. Phys. 12 (2025) 029.
[90] Reginald Christian Bernardo, Seoktae Koh, and Gansukh Tumurtushaa, Implications of pulsar timing arrays for Gauss-Bonnet inflation, J. Cosmol. Astropart. Phys. 10 (2025) 013.
[91] Chris Choi and Tina Kahniashvili, Do pulsar timing datasets favor massive gravity?, arXiv:2507.02059.
[92] Satyabrata Datta and Rome Samanta, Multifaceted supercooling: From PTA to LIGO, J. High Energy Phys. 12 (2025) 161.
[93] Utkarsh Kumar, Primordial gravitational wave background as a probe of the primordial black holes, Phys. Rev. D **112**, 084027 (2025).
[94] Xavier Siemens, Justin Ellis, Fredrick Jenet, and Joseph D. Romano, The stochastic background: Scaling laws and time to detection for pulsar timing arrays, Classical Quantum Gravity **30**, 224015 (2013).
[95] Christopher J. Moore, Stephen R. Taylor, and Jonathan R. Gair, Estimating the sensitivity of pulsar timing arrays, Classical Quantum Gravity **32**, 055004 (2015).
[96] Rutger van Haasteren and Michele Vallisneri, Low-rank approximations for large stationary covariance matrices, as

used in the Bayesian and generalized-least-squares analysis..., Mon. Not. R. Astron. Soc. **446**, 1170 (2015).
[97] Rutger van Haasteren and Michele Vallisneri, New advances in the Gaussian-process approach to pulsar-timing data analysis, Phys. Rev. D **90**, 104012 (2014).
[98] Wenzer Qin, Kimberly K. Boddy, Marc Kamionkowski, and Liang Dai, Pulsar-timing arrays, astrometry, and gravitational waves, Phys. Rev. D **99**, 063002 (2019).
[99] Kin-Wang Ng, Redshift-space fluctuations in stochastic gravitational wave background, Phys. Rev. D **106**, 043505 (2022).
[100] Guo-Chin Liu and Kin-Wang Ng, Timing-residual power spectrum of a polarized stochastic gravitational-wave background in pulsar-timing-array observation, Phys. Rev. D **106**, 064004 (2022).
[101] Bruce Allen, Variance of the Hellings-Downs correlation, Phys. Rev. D **107**, 043018 (2023).
[102] Mesut Çalışkan, Yifan Chen, Liang Dai, Neha Anil Kumar, Isak Stomberg, and Xiao Xue, Dissecting the stochastic gravitational wave background with astrometry, J. Cosmol. Astropart. Phys. 05 (2024) 030.
[103] Alex Kehagias and Antonio Riotto, The PTA Hellings and Downs correlation unmasked by symmetries, J. Cosmol. Astropart. Phys. 06 (2024) 059.
[104] Qiuyue Liang, Ippei Obata, and Misao Sasaki, Testing gravity with frequency-dependent overlap reduction function in Pulsar Timing Array, J. Cosmol. Astropart. Phys. 10 (2024) 097.
[105] Wayne Hu, Qiuyue Liang, Meng-Xiang Lin, and Mark Trodden, Testing gravity with realistic gravitational waveforms in Pulsar Timing Arrays, J. Cosmol. Astropart. Phys. 12 (2024) 054.
[106] Xiao Xue, Zhen Pan, and Liang Dai, Non-Gaussian statistics of nanohertz stochastic gravitational waves, Phys. Rev. D **111**, 043022 (2025).
[107] Bruce Allen, Pulsar timing array harmonic analysis and source angular correlations, Phys. Rev. D **110**, 043043 (2024).
[108] Bruce Allen and Joseph D. Romano, Optimal reconstruction of the Hellings and Downs correlation, Phys. Rev. Lett. **134**, 031401 (2025).
[109] Dustin R. Madison, Orthonormal bases for reconstructing pairwise interpulsar correlations in pulsar timing arrays, Phys. Rev. D **110**, 104066 (2024).
[110] Bruce Allen and Joseph D. Romano, Harmonic spectrum of pulsar timing array angular correlations, arXiv:2412.14852.
[111] Cyril Pitrou and Giulia Cusin, Mitigating cosmic variance in the Hellings-Downs curve: A cosmic microwave background analogy, Phys. Rev. D **111**, 083544 (2025).
[112] Jeffrey S. Hazboun, Joseph D. Romano, and Tristan L. Smith, Realistic sensitivity curves for pulsar timing arrays, Phys. Rev. D **100**, 104028 (2019).
[113] Valentina Di Marco, Andrew Zic, Ryan M. Shannon, and Eric Thrane, Systematic errors in searches for nanohertz gravitational waves, Mon. Not. R. Astron. Soc. **532**, 4026 (2024).
[114] Gabriella Agazie *et al.* (NANOGrav Collaboration), The NANOGrav 15 yr dataset: Posterior predictive checks for gravitational-wave detection with pulsar timing arrays, Phys. Rev. D **111**, 042011 (2025).
[115] Boris Goncharov, Shubhit Sardana, A. Sesana, J. Antoniadis, A. Chalumeau, D. Champion, S. Chen, E. F. Keane, G. Shaifullah, and L. Speri, Reading signatures of supermassive binary black holes in pulsar timing array observations, Nat. Commun. **16**, 9692 (2025).
[116] Boris Goncharov and Shubhit Sardana, Ensemble noise properties of the European Pulsar Timing Array, Mon. Not. R. Astron. Soc. **537**, 3470 (2025).
[117] Reginald Christian Bernardo and Kin-Wang Ng, Accurate pulsar timing array residual variances and correlation of the stochastic gravitational wave background, Phys. Rev. D **113**, L021501 (2026).
[118] Marco Crisostomi, Rutger van Haasteren, Patrick M. Meyers, and Michele Vallisneri, Beyond diagonal approximations: Improved covariance modeling for pulsar timing array data analysis, arXiv:2506.13866.
[119] Bruce Allen, Arian L. von Blanckenburg, and Ken D. Olum, Pulsar timing array analysis in a Legendre polynomial basis, arXiv:2510.05913.
[120] Y. Akrami *et al.* (Planck Collaboration), Planck 2018 results. X. Constraints on inflation, Astron. Astrophys. **641**, A10 (2020).
[121] Y. Akrami *et al.* (Planck Collaboration), Planck 2018 results. VII. Isotropy and Statistics of the CMB, Astron. Astrophys. **641**, A7 (2020).
[122] Reginald Christian Bernardo, Stephen Appleby, and Kin-Wang Ng, Toward a test of Gaussianity of a gravitational wave background, J. Cosmol. Astropart. Phys. 01 (2025) 017.
[123] Michele Maggiore, *Gravitational Waves. Vol. 2: Astrophysics and Cosmology* (Oxford University Press, New York, 2018).
[124] N. M. Jiménez Cruz, Ameek Malhotra, Gianmassimo Tasinato, and Ivonne Zavala, Measuring kinematic anisotropies with pulsar timing arrays, Phys. Rev. D **110**, 063526 (2024).
[125] N. M. Jiménez Cruz, Ameek Malhotra, Gianmassimo Tasinato, and Ivonne Zavala, Measuring the circular polarization of gravitational waves with pulsar timing arrays, Phys. Rev. D **110**, 103505 (2024).
[126] G. Hobbs, F. Jenet, K. J. Lee, J. P. W. Verbiest, D. Yardley, R. Manchester, A. Lommen, W. Coles, R. Edwards, and C. Shettigara, TEMPO2, a new pulsar timing package. III: Gravitational wave simulation, Mon. Not. R. Astron. Soc. **394**, 1945 (2009).
[127] Chiara M. F. Mingarelli, Trevor Sidery, Ilya Mandel, and Alberto Vecchio, Characterizing gravitational wave stochastic background anisotropy with pulsar timing arrays, Phys. Rev. D **88**, 062005 (2013).
[128] Ryo Kato and Jiro Soda, Probing circular polarization in stochastic gravitational wave background with pulsar timing arrays, Phys. Rev. D **93**, 062003 (2016).
[129] Enis Belgacem and Marc Kamionkowski, Chirality of the gravitational-wave background and pulsar-timing arrays, Phys. Rev. D **102**, 023004 (2020).
[130] Gabriela Sato-Polito and Marc Kamionkowski, Pulsar-timing measurement of the circular polarization of the

stochastic gravitational-wave background, Phys. Rev. D **106**, 023004 (2022).
[131] Yu-Kuang Chu, Guo-Chin Liu, and Kin-Wang Ng, Observation of a polarized stochastic gravitational-wave background in pulsar-timing-array experiments, Phys. Rev. D **104**, 124018 (2021).
[132] Reginald Christian Bernardo and Kin-Wang Ng, Charting the nanohertz gravitational wave sky with pulsar timing arrays, Int. J. Mod. Phys. D **34**, 2540013 (2025).
[133] Rutger van Haasteren, Yuri Levin, Patrick McDonald, and Tingting Lu, On measuring the gravitational-wave background using Pulsar Timing Arrays, Mon. Not. R. Astron. Soc. **395**, 1005 (2009).
[134] Lindley Lentati, P. Alexander, M. P. Hobson, S. Taylor, J. Gair, S. T. Balan, and R. van Haasteren, Hyper-efficient model-independent Bayesian method for the analysis of pulsar timing data, Phys. Rev. D **87**, 104021 (2013).
[135] Adrian Boîtier, Tanguy Giroud, Shubhanshu Tiwari, and Philippe Jetzer, Series expansion of the overlap reduction function for scalar and vector polarizations for gravitational wave search with pulsar timing arrays, Phys. Rev. D **105**, 084006 (2022).
[136] R. K. Sachs and A. M. Wolfe, Perturbations of a cosmological model and angular variations of the microwave background, Astrophys. J. **147**, 73 (1967).
[137] Guillem Domènech and Apostolos Tsabodimos, Finite distance effects on the Hellings–Downs curve in modified gravity, Eur. Phys. J. C **84**, 1005 (2024); Eur. Phys. J. C **84**, 1123(E) (2024).
[138] Jonathan Gair, Joseph D. Romano, Stephen Taylor, and Chiara M. F. Mingarelli, Mapping gravitational-wave backgrounds using methods from CMB analysis: Application to pulsar timing arrays, Phys. Rev. D **90**, 082001 (2014).
[139] Chiara M. F. Mingarelli and Angelo B. Mingarelli, Proving the short-wavelength approximation in Pulsar Timing Array gravitational-wave background searches, J. Phys. Comm. **2**, 105002 (2018).
[140] Paul Frederik Depta, Valerie Domcke, Gabriele Franciolini, and Mauro Pieroni, Pulsar timing array sensitivity to anisotropies in the gravitational wave background, Phys. Rev. D **111**, 083039 (2025).
[141] George Hobbs, R. Edwards, and R. Manchester, Tempo2, a new pulsar timing package. 1. Overview, Mon. Not. R. Astron. Soc. **369**, 655 (2006).
[142] Russell T. Edwards, G. B. Hobbs, and R. N. Manchester, Tempo2, a new pulsar timing package. 2. The timing model and precision estimates, Mon. Not. R. Astron. Soc. **372**, 1549 (2006).
[143] Reginald Christian Bernardo and Kin-Wang Ng, PTAfast: PTA correlations from stochastic gravitational wave background, Astrophysics Source Code Library, record ascl:2211.001 (2022).
[144] Matthew T. Miles *et al.*, The MeerKAT Pulsar Timing Array: First data release, Mon. Not. R. Astron. Soc. **519**, 3976 (2023).
[145] Matthew T. Miles *et al.*, The MeerKAT Pulsar Timing Array: The 4.5-year data release and the noise and stochastic signals of the millisecond pulsar population, Mon. Not. R. Astron. Soc. **536**, 1467 (2025).
[146] Selim C. Hotinli, Marc Kamionkowski, and Andrew H. Jaffe, The search for anisotropy in the gravitational-wave background with pulsar-timing arrays, Open J. Astrophys. **2**, 8 (2019).
[147] Nathan J. Secrest, Sebastian von Hausegger, Mohamed Rameez, Roya Mohayaee, Subir Sarkar, and Jacques Colin, A test of the cosmological principle with quasars, Astrophys. J. Lett. **908**, L51 (2021).
[148] Nathan J. Secrest, Sebastian von Hausegger, Mohamed Rameez, Roya Mohayaee, and Subir Sarkar, A challenge to the standard cosmological model, Astrophys. J. Lett. **937**, L31 (2022).
[149] Lawrence Dam, Geraint F. Lewis, and Brendon J. Brewer, Testing the cosmological principle with CatWISE quasars: A Bayesian analysis of the number-count dipole, Mon. Not. R. Astron. Soc. **525**, 231 (2023).
[150] Oliver T. Oayda, Vasudev Mittal, Geraint F. Lewis, and Tara Murphy, A Bayesian approach to the cosmic dipole in radio galaxy surveys: Joint analysis of NVSS & RACS, Mon. Not. R. Astron. Soc. **531**, 4545 (2024).
[151] Sebastian von Hausegger, The expected kinematic matter dipole is robust against source evolution, Mon. Not. R. Astron. Soc. **535**, L49 (2024).
[152] Akhil Antony, Stephen Appleby, William L. Matthewson, and Arman Shafieloo, Isotropy test with quasars using method of smoothed residuals, J. Cosmol. Astropart. Phys. 01 (2026) 001.
[153] Nathan Secrest, Sebastian von Hausegger, Mohamed Rameez, Roya Mohayaee, and Subir Sarkar, Colloquium: The cosmic dipole anomaly, Rev. Mod. Phys. **97**, 041001 (2025).
[154] Jaiyul Yoo, Matteo Magi, and Dragan Huterer, Cosmic dipoles from large-scale structure surveys, Phys. Rev. D **112**, 123013 (2025).
[155] Gianmassimo Tasinato, Kinematic anisotropies and pulsar timing arrays, Phys. Rev. D **108**, 103521 (2023).
[156] Reginald Christian Bernardo and Kin-Wang Ng, Stochastic gravitational wave background phenomenology in a pulsar timing array, Phys. Rev. D **107**, 044007 (2023).
[157] Reginald Christian Bernardo, Guo-Chin Liu, and Kin-Wang Ng, Correlations for an anisotropic polarized stochastic gravitational wave background in pulsar timing arrays, J. Cosmol. Astropart. Phys. 04 (2024) 034.
[158] Yacine Ali-Haïmoud, Tristan L. Smith, and Chiara M. F. Mingarelli, Insights into searches for anisotropies in the nanohertz gravitational-wave background, Phys. Rev. D **103**, 042009 (2021).
[159] Gabriella Agazie *et al.* (NANOGrav Collaboration), The NANOGrav 15 yr data set: Search for anisotropy in the gravitational-wave background, Astrophys. J. Lett. **956**, L3 (2023).
[160] Elinore Roebber and Gilbert Holder, Harmonic space analysis of pulsar timing array redshift maps, Astrophys. J. **835**, 21 (2017).
[161] Bruce Allen and Joseph D. Romano, Hellings and Downs correlation of an arbitrary set of pulsars, Phys. Rev. D **108**, 043026 (2023).
[162] Reginald Christian Bernardo and Kin-Wang Ng, Pulsar and cosmic variances of pulsar timing-array correlation

measurements of the stochastic gravitational wave background, J. Cosmol. Astropart. Phys. 11 (2022) 046.
[163] P. C. Peters, Gravitational radiation and the motion of two point masses, Ph.D. thesis, Caltech, 1964.
[164] Lorenz Zwick, Pedro R. Capelo, Elisa Bortolas, Lucio Mayer, and Pau Amaro-Seoane, Improved gravitational radiation time-scales: Significance for LISA and LIGO-Virgo sources, Mon. Not. R. Astron. Soc. **495**, 2321 (2020).
[165] Charles Dalang and Camille Bonvin, On the kinematic cosmic dipole tension, Mon. Not. R. Astron. Soc. **512**, 3895 (2022).
[166] Eleonora Di Valentino *et al.* (CosmoVerse Network Collaboration), The CosmoVerse White Paper: Addressing observational tensions in cosmology with systematics and fundamental physics, Phys. Dark Universe **49**, 101965 (2025).
[167] J. D. Wagenveld, S. von Hausegger, H-R. Klöckner, and D. J. Schwarz, The kinematic contribution to the cosmic number count dipole, Astron. Astrophys. **697**, A112 (2025).
[168] William DeRocco and Jeff A. Dror, Using pulsar parameter drifts to detect subnanohertz gravitational waves, Phys. Rev. Lett. **132**, 101403 (2024).
[169] William DeRocco and Jeff A. Dror, Searching for stochastic gravitational waves below a nanohertz, Phys. Rev. D **108**, 103011 (2023).
[170] D. A. Varshalovich, A. N. Moskalev, and V. K. Khersonskii, *Quantum Theory of Angular Momentum* (World Scientific, Singapore, 1988), https://www.worldscientific.com/doi/pdf/10.1142/0270.
[171] Stanislav Babak, Mikel Falxa, Gabriele Franciolini, and Mauro Pieroni, Forecasting the sensitivity of pulsar timing arrays to gravitational wave backgrounds, Phys. Rev. D **110**, 063022 (2024).